Probabilistic linear inversion of satellite gravity gradient data applied to the northeast Atlantic

A. Minakov, C. Gaina[1]

[1]Centre for Earth Evolution and Dynamics, University of Oslo, Norway

Key Points:

- We present a methodology for 3-D linear inversion of satellite gravity gradient data using statistical prior information
- We apply the inversion method to estimate the density variation in the upper mantle beneath the northeast Atlantic Ocean
- The predicted density variations are compared to independent results of seismic tomography and linked to distribution of Cenozoic underwater volcanoes and seamount-like features of the seafloor

Corresponding author: A. Minakov, alexander.minakov@geo.uio.no

Abstract

We explore the mantle density structure of the northeast Atlantic region using constrained linear inversion of the satellite gravity gradient data based on statistical prior information and assuming a Gaussian model. The uncertainty of residual gravity gradient signal is characterized by covariance matrix obtained using geostatistical analysis of controlled-source seismic data. The forward modeling of the gravity gradients in the 3D reference crustal model is performed using a global spherical harmonics analysis. We estimate the model covariance function in the radial and angular directions using a variogram method. We compute volumetric gravity gradient kernels for a spherical shell covering the northeast Atlatic region down to the mantle transition zone (410 km depth). The solution of the linear inverse problem in the form the mean density model follows a least-squares approach. The results indicate a direct relation between the seismic velocity and density anomalies in the Iceland-Jan Mayen region, Greenland and the Norwegian passive margin. The predicted low-density anomalies at the depth of 100-150 km underneath the northeast Atlantic Ocean are correlated with the distribution of Cenozoic underwater volcanoes and seamount-like features of the seafloor.

Plain Language Summary

We image density heterogeneities within the upper 400-km layer of the Earth beneath Greenland and the northeast Atlantic region using satellite gravity gradient data. The observed density anomalies within continental and oceanic lithosphere are linked to the activity of Iceland plume throughout the Cenozoic time (0-60 Ma).

1 Introduction

The GOCE satellite mission was active during 2009-2013 and provided global coverage with gravity tensor data (Fig. 1) (European Space Agency, `https://earth.esa.int/`). Unlike other gravity missions, the GOCE gravity measurements were made directly at the orbit (220-250 km height). The spatial derivatives of gravitational potential help to enhance the signal from lithospheric sources. The GOCE observation level acts as a natural upward continuation filter suppressing a high-frequency "noise" due to superficial structures and enhancing the spectral band of the gravity field linked to the density variation in the upper mantle (Sebera et al., 2017).

The present-day configuration of the lithosphere in the northeast Atlantic is the result of continental rifting, break-up and subsequent seafloor spreading that formed the oceanic basin from about 56 Ma (Gaina, Nasuti, et al., 2017) (Fig. 2). It is postulated that seafloor spreading was initiated after the North Atlantic Igneous Province (NAIP) (e.g. R. White & McKenzie, 1989) was emplaced affecting a substantial part of the Greenland and Eurasia lithosphere. The geodynamic evolution of the northeast Atlantic over the subsequent 50 myr may have developed in a pulsating fashion with periods of high and low magmatic and tectonic activity as documented in Iceland, mid-ocean ridges (Ito, 2001; Jones et al., 2002; Parnell-Turner et al., 2014), by pervasive seamount volcanism (Gaina, Blischke, et al., 2017) and episodic uplift and basin inversion at the passive continental margins (N. White & Lovell, 1997; Rudge et al., 2008).

The early evolution of the northeast Atlantic was inferred from a number of seismic reflection and refraction profiles, mostly at the continent-ocean transition. Both intrusives and extrusive magmatic rocks associated with NAIP has been mapped in detail (Eldholm & Grue, 1994). Variable physical properties of the igneous crust in the deep ocean basin were linked to the Miocene activity of the Iceland hotspot (Parkin & White, 2008; A. J. Breivik et al., 2008). Iceland is presently in the vicinity of the active Mid-Atlantic Ridge, and has been a ridge-centered mantle melt anomaly during late Cenozoic (Ito, 2001). Several studies have recently proposed that basaltic upper crust can be

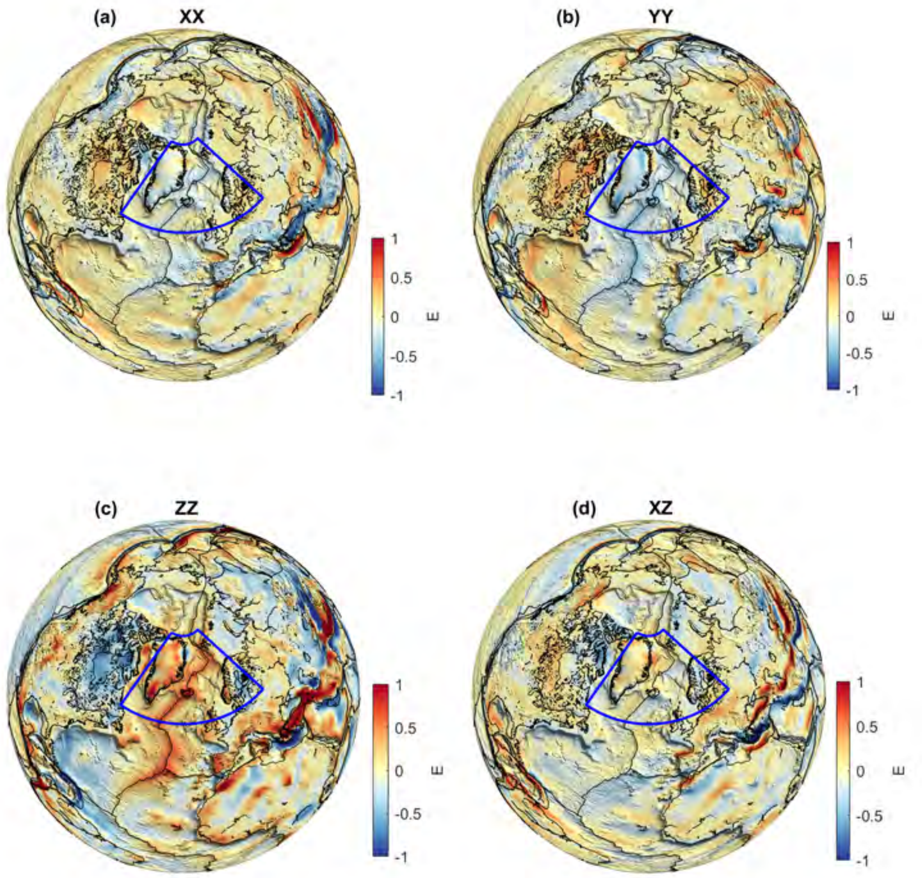

Figure 1. GOCE gravity gradients (a) XX-, (b) YY-, (c) ZZ-, and (d) XZ-components.

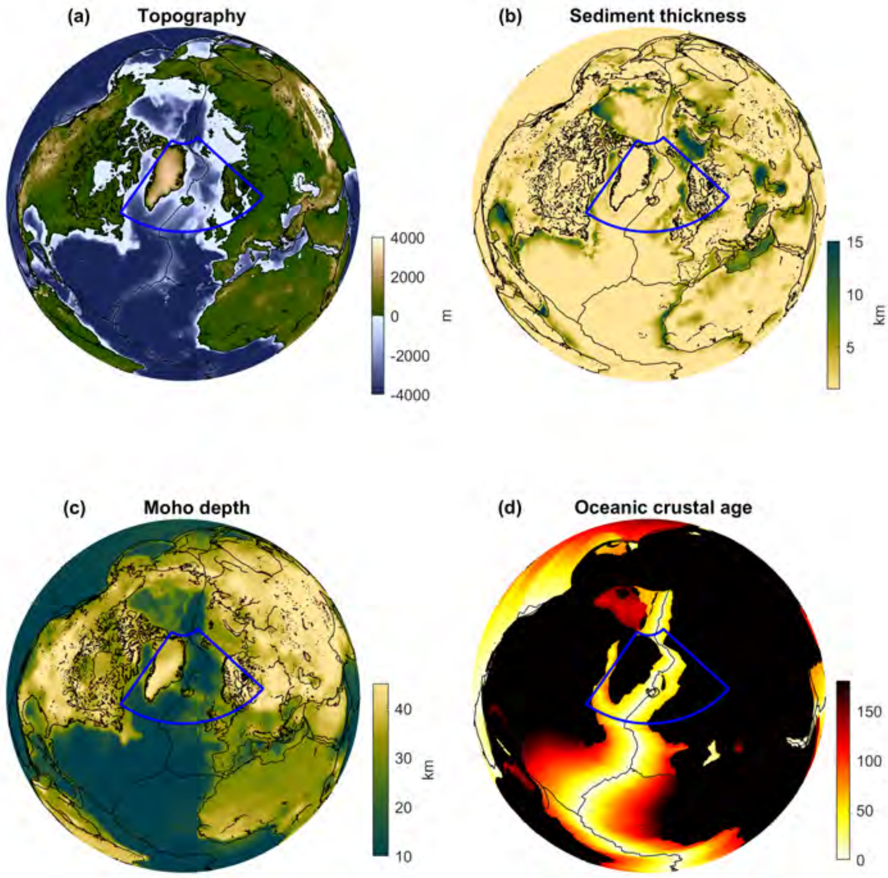

Figure 2. Data-set compilations used in this work: (a) Topography (GEBCO, 2019), (b) Sediment thickness (Straume et al., 2019), (c) Moho depth (Szwillus et al., 2019; Funck et al., 2017), and (d) Crustal age (Gaina, Nasuti, et al., 2017) . The blue sector indicates the northeast Atlantic study region.

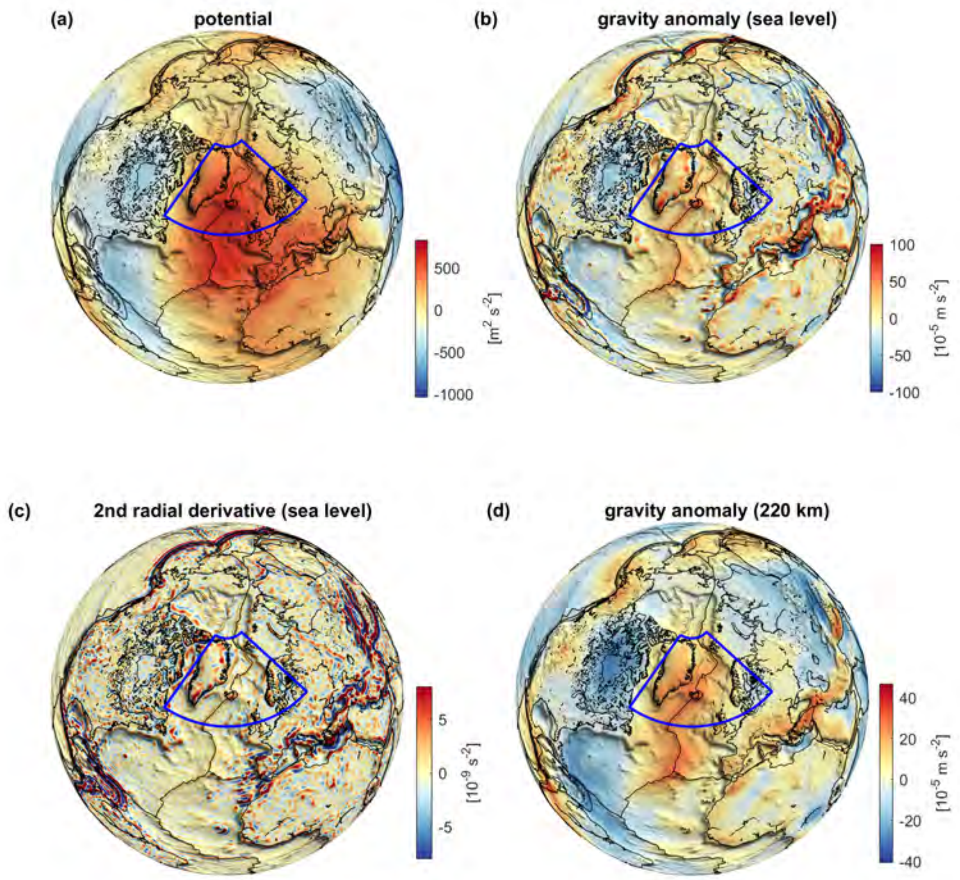

Figure 3. GOCE-derived datasets (a) Gravitational potential anomaly, (b) free-air gravity anomaly (at sea level), (c) radial gravity gradient at sea level, and (d) gravity anomaly (at 220-km height). The blue sector indicates the northeast Atlantic study region. GEBCO topography/bathymetry grid (GEBCO, 2019) is used as shaded relief surface.

underlain by extended continental crustal reworked by intrusive magmatism (Torsvik et al., 2015; Foulger et al., 2019). Petrological models suggest that the mantle source of Iceland lavas is a peridotite (80-90%) mixed with basalt (10-20%), and would imply a density perturbation of 10-20 $\mathrm{kg\,m^{-3}}$ (Brown & Lesher, 2014). However, the density distribution within the primary melt source region in the upper mantle remains unknown.

The long-term magmatic and tectonic evolution of the northeast Atlantic region are controlled by processes in the mantle. The present-day mantle density variation provide important constraints for evolutionary dynamic models and useful for quantitative understanding of the stress regime in the shallow upper crust. The northeast Atlantic region is associated with a broad and intense high of the gravitational potential attributed by a superposition of shallow and deep mantle heterogeneities (Fig. 3 ; Cochran and Talwani (1978)), and disentangling these anomalous density sources is not fully possible due to non-uniqueness of the inverse gravimetric problem. Moreover, the surface topography and crustal thickness variation is known to constitute of up to 80 % of the observed gravity signal (Sebera et al., 2017). To better utilize the physical constraints provided by gravity data, it is important to assess the contribution of individual density sources (with a presumably known probability) and provide a statistical measure for the uncertainty of the final density model.

The density variation beneath hotspot regions is a key physical parameter for understanding thermo-chemical convection and distribution of volcanism. At the same time, a parametric relation between the seismic velocity and density in non-adiabatic and partially molten upper mantle is not available. There have been few attempts to directly invert the gravity gradient data directly due to non-uniqueness of the solution. Here, we suggest a method to utilize the prior information in the 3-D sphere in the form of: i) data covariance matrix; ii) prior model covariance matrix including a model for spatial variability of mantle heterogeneity: and iii) a stabilizing functional in the form of spatial weighting function. We construct a seismically-constrained 3D crustal reference model including ice, water, sediments, and crystalline crustal layers based on spherical kriging interpolation (Fig. 2) including a model for the average density of the crystalline crust. Then, we use the GOCE grids to infer density variation (and associated Gaussian probability distribution) in the upper mantle in a spherical shell within the northeast Atlantic region based on constrained linear inversion of gravity gradient data using statistical prior information.

2 Data and Methodology

The density structure of the lithosphere and asthenosphere in the northeast Atlantic region based on the gravity data has been previously addressed in a number of studies (Haase et al., 2016; Tan et al., 2018; Shulgin & Artemieva, 2019). Tan et al. (2018) focuses on the lithospheric density structure of the oceanic region around Jan Mayen island and discuss possible impact of the Iceland hotspot on the temperature and density structure in this region. Shulgin and Artemieva (2019) performed density modeling using a tesseroid approach to discuss thermochemical structure of the upper mantle. As constraints, they used the UNASeis crustal model of Artemieva and Thybo (2013). A spectral method based on global spherical harmonics analysis, combined with local isostasy constraints, has been applied by B. Root (2020) to investigate the relation between seismic velocity and density structure of the lithosphere.

A population of acceptable solutions of the potential fields inverse problem requires a priori constraints and regularization. Zhdanov (2015) discussed various stabilizing functionals applied to model parameters which can be instrumental to obtain a solution satisfying certain a priori geological or geophysical knowledge, such as the minimum-norm, maximum smoothness, total variation, minimum entropy and minimum-gradient support functionals (Last & Kubik, 1983; Portniaguine & Zhdanov, 1999; Boulanger & Chouteau, 2001). Li and Oldenburg (1996) suggested a stabilizing function for the potential field inversion in the form of the inverse distance ($1/r^{\beta}$) to counteract the rapid decay with distance of the integral kernels. Zhdanov et al. (2011) and Wan and Zhdanov (2013) proposed a method for rapid imaging using gravity gradient data incorporating the depth weighting of Li and Oldenburg (1996) and a known background density model. Chasseriau and Chouteau (2003); Barnoud et al. (2016) considered the inverse gravity problem in a Bayesian formulation implying that the density variation and the observed data can be considered as Gaussian random fields characterized by their mean and the covariance matrix.

The 3D gravity gradient inversion method has been traditionally used in mineral and petroleum exploration focusing on the reconstruction of localized density anomalies e.g. (Pilkington, 2014; Wan & Zhdanov, 2013). For a particular case of point mass sources or weakly interfering localized sources, the eigenvectors of the gravity gradient tensor indicate the direction to the location of point mass (or baricenters of localized bodies) (Pedersen & Rasmussen, 1990; Mikhailov et al., 2007). In general, the vertical (radial) component of the gravitational tensor is shown to be most informative and often utilized (Pilkington, 2014).

In these previous studies the analysis has been performed for models in Cartesian coordinates. The applications at a lithospheric or planetary scale are less common and specifically require a consistency between model parameterization and observation reference frames. Liang et al. (2014) used a tesseroid approach and performed linear inversion using a combination of angular and radial weighting functions as constraints. Afonso et al. (2019) performed constrained non-linear inversion of GOCE gradients (together with other geophysical constraints) for several lithospheric layers. An efficient method for forward and inverse gravity modeling of crustal density structure based on spherical harmonic analysis was introduced by Wieczorek and Phillips (1998). Novák and Grafarend (2006) and B. C. Root et al. (2015) have further extended this method for various geophysical applications. Martinec and Fullea (2015) used the GOCE gravity gradient data to model density structure of the Congo basin based on a spherical harmonic approach.

The modeling method presented in this study combines the computationally efficient spherical harmonics method and the local parameterization to perform a probabilistic linear inversion of satellite gravity gradient data in spherical coordinates. The input GOCE data have the form of grids in the local (north-oriented) reference frame (LNOF) (Bouman et al., 2015). The gravity field solutions (grids) contain a detailed signal at a height of $\approx$ 220 km with a spatial resolution of $\approx$ 80 km (Fig. 1).

2.1 Preliminaries

The gravity vector can be expressed using a scalar potential as

$$\mathbf{g}(\mathbf{r}) = \nabla U(\mathbf{r}). \tag{1}$$

The gravitation tensor is defined as double gradient of the gravitational potential

$$\mathbf{T}(\mathbf{r}) = \nabla\nabla U(\mathbf{r}). \tag{2}$$

The gravitational potential due to density distribution $\rho(\mathbf{r}')$ at point $\mathbf{r}$ can be computed using the volume integral

$$U(\mathbf{r}) = \gamma \int_V \rho(\mathbf{r}')G(\mathbf{r},\mathbf{r}')\mathrm{dV} \tag{3}$$

where γ is the gravitational constant. The scalar Green function G is in the form of inverse distance function:

$$G(\mathbf{r},\mathbf{r}') = \frac{1}{|\mathbf{r}-\mathbf{r}'|}. \tag{4}$$

The integral forms for the gravity vector and gravity gradient tensor can be obtained by substituting eq. 3 in eqs 1 and 2

$$\mathbf{g}(\mathbf{r}) = \gamma \int_V \rho(\mathbf{r}')\nabla G(\mathbf{r},\mathbf{r}')\mathrm{dV} \tag{5}$$

$$\mathbf{T}(\mathbf{r}) = \gamma \int_V \rho(\mathbf{r}')\nabla\nabla G(\mathbf{r},\mathbf{r}')\mathrm{dV} \tag{6}$$

The ways of solving the integrals 3, 5 and 6 depend on application.

In Cartesian coordinates

$$
\begin{aligned}
|\mathbf{r}-\mathbf{r}'| &= \sqrt{(\mathbf{x}-\mathbf{x}')^2+(\mathbf{y}-\mathbf{y}')^2+(\mathbf{z}-\mathbf{z}')^2} && (7)\\
\rho(\mathbf{r}') &= \rho(\mathbf{x}',\mathbf{y}',\mathbf{z}') && (8)\\
dV &= dxdydz && (9)
\end{aligned}
$$

The geocentric latitude, longitude and radial distance are related to Cartesian coordinates as

$$
\begin{aligned}
x &= r\cos\phi\cos\lambda && (10)\\
y &= r\cos\phi\sin\lambda && (11)\\
z &= r\sin\phi && (12)
\end{aligned}
$$

The angular distance ψ between vectors $\mathbf{r}$ and $\mathbf{r}'$ can be expressed using spherical coordinates

$$
\cos\psi = \frac{\mathbf{r}\cdot\mathbf{r}'}{|\mathbf{r}||\mathbf{r}'|} = \sin\phi\sin\phi' + \cos\phi\cos\phi'\cos(\lambda-\lambda'). \tag{13}
$$

The following relation can be used in the integral eq. 3

$$
\begin{aligned}
|\mathbf{r}-\mathbf{r}'| &= \sqrt{|\mathbf{r}|^2+|\mathbf{r}'|^2-2|\mathbf{r}||\mathbf{r}'|\cos\psi} && (14)\\
\rho(\mathbf{r}') &= \rho(|\mathbf{r}'|,\phi',\lambda') && (15)\\
dV &= |\mathbf{r}'|^2\cos\phi' drd\phi d\lambda && (16)
\end{aligned}
$$

The gradient operation expressed using a non-Cartesian basis $\mathbf{e}^j$ is

$$
\nabla U = h_j^{-1}\mathbf{e}^j\frac{\partial U}{\partial x^j} \tag{17}
$$

where h_j are the normalization coefficients which for spherical coordinates are $h_r = 1$, $h_\phi = r$, and $h_\lambda = r\cos\phi$.

The double gradient operation in dyadic notation becomes

$$
\begin{aligned}
\nabla\nabla U &= h_i^{-1}\mathbf{e}^i\frac{\partial}{\partial x^i}\left(h_j^{-1}\mathbf{e}^j\frac{\partial U}{\partial x^j}\right)\\
&= h_i^{-1}\mathbf{e}^i\left(\mathbf{e}^j\frac{\partial h_j^{-1}}{\partial x^i}\frac{\partial U}{\partial x^j} + h_j^{-1}\frac{\partial \mathbf{e}^j}{\partial x^i}\frac{\partial U}{\partial x^j} + h_j^{-1}\mathbf{e}^j\frac{\partial^2 U}{\partial x^i\partial x^j}\right). && (18)
\end{aligned}
$$

The derivatives of the basis vectors $\mathbf{e}^i \rightarrow (\mathbf{e}_r,\mathbf{e}_\phi,\mathbf{e}_\lambda)$ (radial outward, north, east direction) with respect to spherical coordinates $x^i \rightarrow (r,\phi,\lambda)$:

$$
\frac{\partial(\mathbf{e}_r,\mathbf{e}_\phi,\mathbf{e}_\lambda)}{(r,\phi,\lambda)} = \begin{pmatrix} 0 & \mathbf{e}_\phi & \mathbf{e}_\lambda\cos\phi \\ 0 & -\mathbf{e}_r & -\mathbf{e}_\lambda\sin\phi \\ 0 & 0 & -\mathbf{e}_r\cos\phi+\mathbf{e}_\phi\sin\phi \end{pmatrix} \tag{19}
$$

2.2 Global spherical harmonic analysis and topographic sources

The scalar Green function G can be expressed using spherical harmonics

$$
G(\mathbf{r},\mathbf{r}') = \frac{1}{|\mathbf{r}-\mathbf{r}'|} = \frac{1}{r}\sum_{n=0}^{\infty}\frac{1}{2n+1}\left(\frac{r'}{r}\right)^n\sum_{m=-n}^{n}Y_{n,m}(\hat{\mathbf{r}})Y^*_{n,m}(\hat{\mathbf{r}}') \tag{20}
$$

where $\mathbf{r} = r\hat{\mathbf{r}}$, $\mathbf{r}' = r'\hat{\mathbf{r}}'$, $\hat{\mathbf{r}}' = [\cos\phi'\cos\lambda', \cos\phi'\sin\lambda', \sin\phi']^T$.

We substitute this equation in eq. 3 together with eqs 15 and 16.

$$\begin{aligned} U &= \gamma \sum_{n=0}^{\infty} \sum_{m=-n}^{n} \frac{1}{2n+1} \left(\frac{1}{r}\right)^{n+1} Y_{n,m}(\hat{\mathbf{r}}) \times \\ &\times \int_{-\pi/2}^{\pi/2} \int_{-\pi}^{\pi} \rho(\hat{\mathbf{r}}') Y^*_{n,m}(\hat{\mathbf{r}}) \cos\phi d\phi d\lambda \int_{R_0+h_1}^{R_0+h_2} r'^{n+2} dr \end{aligned} \quad (21)$$

Approximating the radial integral by the first three terms of Taylor series, we obtain

$$\begin{aligned} U &= \gamma \sum_{n=0}^{\infty} \sum_{m=-n}^{n} \frac{R_0^{n+3}}{2n+1} \left(\frac{1}{r}\right)^{n+1} Y_{n,m}(\hat{\mathbf{r}}) \times \\ &\times \int_{-\pi/2}^{\pi/2} \int_{-\pi}^{\pi} F(\hat{\mathbf{r}}') Y^*_{n,m}(\hat{\mathbf{r}}') \cos\phi d\phi d\lambda \end{aligned} \quad (22)$$

where $F(\hat{\mathbf{r}}')$ is defined as

$$F = \frac{\rho}{R_0}(h_2 - h_1) + \frac{(n+2)}{R_0^2}(h_2^2 - h_1^2)\rho + \frac{(n+2)(n+1)}{R_0^3}(h_2^3 - h_1^3)\rho. \quad (23)$$

Here, $h_1(\phi, \lambda)$, $h_2(\phi, \lambda)$ describe the bottom and top boundary topography of the spherical layer with density $\rho(\phi, \lambda)$, R_0 is the reference radius.

$F(\hat{\mathbf{r}}')$ can be expanded in spherical harmonics with coefficients $F_{n,m}$:

$$F(\hat{\mathbf{r}}') = \sum_{n=0}^{\infty} \sum_{m=-n}^{n} F_{n,m} Y_{n,m}(\hat{\mathbf{r}}') \quad (24)$$

Substituting eq. (24) into eq. (22) and using the orthogonality property of spherical harmonics, we obtain

$$U(r, \hat{\mathbf{r}}) = \gamma R_0^2 \sum_{n=0}^{\infty} \sum_{m=-n}^{n} \frac{4\pi}{2n+1} \left(\frac{R_0}{r}\right)^{n+1} F_{n,m} Y_{n,m}(\hat{\mathbf{r}}) \quad (25)$$

The external gravitational potential in geocentric spherical coordinates can be represented in terms of surface spherical harmonics:

$$U(r, \hat{\mathbf{r}}) = \frac{\gamma M}{R} \sum_{n=0}^{\infty} \sum_{m=-n}^{n} \left(\frac{R}{r}\right)^{n+1} \overline{C}_{n,m} Y_{n,m}(\hat{\mathbf{r}}) \quad (26)$$

where $M = 4\pi\rho_E R^3/3$ is the total mass of the Earth with the average density of ρ_E, R is the reference radius, and $\overline{C}_{n,m}$ are fully normalized spherical harmonic coefficients.

The Stokes coefficients for the gravitational potential can be obtained by equating these two equations:

$$\overline{C}_{n,m} = \frac{3}{\rho_E(2n+1)} \left(\frac{R_0}{R}\right)^{n+3} F_{n,m}. \quad (27)$$

The first and second spatial derivatives of the gravitational potential with respect to spherical coordinates can be obtained in the spectral domain. In particular, the first and second radial derivatives are

$$\frac{\partial U}{\partial r} = \frac{\gamma M}{R^2} \sum_{n=0}^{\infty} \sum_{m=-n}^{n} (n+1) \left(\frac{R}{r} \right)^{n+2} \overline{C}_{n,m} Y_{n,m}(\hat{\mathbf{r}}) \tag{28}$$

$$\frac{\partial^2 U}{\partial r^2} = \frac{\gamma M}{R^3} \sum_{n=0}^{\infty} \sum_{m=-n}^{n} (n+2)(n+1) \left(\frac{R}{r} \right)^{n+3} \overline{C}_{n,m} Y_{n,m}(\hat{\mathbf{r}}) \tag{29}$$

The radial-latitudinal cross-derivative is

$$\frac{\partial^2 U}{\partial r \partial \phi} = \frac{\gamma M}{R^2} \sum_{n=0}^{\infty} \sum_{m=-n}^{n} (n+1) \left(\frac{R}{r} \right)^{n+2} \overline{C}_{n,m} D_\phi Y_{n,m}(\hat{\mathbf{r}}). \tag{30}$$

This expression involves differentiation of spherical harmonics $D_\phi Y_{n,m}$ which can be obtained by standard recursion relations.

The physical components of the gravity gradient tensor can be obtained by substituting the derivatives with respect to the spherical coordinates into eq. 18. The gradient operation applied twice provides the gravity gradient tensor expressed in a local coordinate frame :

$$\begin{aligned}
\nabla\nabla U(\mathbf{r}, \mathbf{r}') &= \nabla \left(\frac{\partial U}{\partial r} \mathbf{e}_r + \frac{1}{r} \frac{\partial U}{\partial \phi} \mathbf{e}_\phi + \frac{1}{r \cos\phi} \frac{\partial U}{\partial \lambda} \mathbf{e}_\lambda \right) = \frac{\partial^2 U}{\partial r^2} \mathbf{e}_r \mathbf{e}_r + \left(\frac{1}{r^2} \frac{\partial^2 U}{\partial \phi^2} + \frac{1}{r} \frac{\partial U}{\partial r} \right) \mathbf{e}_\phi \mathbf{e}_\phi \\
&+ \left(\frac{1}{r^2 \cos^2\phi} \frac{\partial^2 U}{\partial \lambda^2} + \frac{1}{r} \frac{\partial U}{\partial r} - \frac{\sin\phi}{r^2 \cos\phi} \frac{\partial U}{\partial \phi} \right) \mathbf{e}_\lambda \mathbf{e}_\lambda + \\
&+ \left(\frac{1}{r} \frac{\partial^2 U}{\partial \phi \partial r} - \frac{1}{r^2} \frac{\partial U}{\partial \phi} \right) \mathbf{e}_\phi \mathbf{e}_r + \left(\frac{1}{r} \frac{\partial^2 U}{\partial \phi \partial r} - \frac{1}{r^2} \frac{\partial U}{\partial \phi} \right) \mathbf{e}_r \mathbf{e}_\phi \\
&+ \left(\frac{1}{r \cos\phi} \frac{\partial^2 U}{\partial \lambda \partial r} - \frac{1}{r^2 \cos\phi} \frac{\partial U}{\partial \lambda} \right) \mathbf{e}_\lambda \mathbf{e}_r + \left(\frac{1}{r \cos\phi} \frac{\partial^2 U}{\partial \lambda \partial r} - \frac{1}{r^2 \cos\phi} \frac{\partial U}{\partial \lambda} \right) \mathbf{e}_r \mathbf{e}_\lambda \\
&+ \left(\frac{1}{r^2 \cos\phi} \frac{\partial^2 U}{\partial \lambda \partial \phi} + \frac{\sin\phi}{r^2 \cos^2\phi} \frac{\partial U}{\partial \lambda} \right) \mathbf{e}_\lambda \mathbf{e}_\phi + \left(\frac{1}{r^2 \cos\phi} \frac{\partial^2 U}{\partial \lambda \partial \phi} + \frac{\sin\phi}{r^2 \cos^2\phi} \frac{\partial U}{\partial \lambda} \right) \mathbf{e}_\phi \mathbf{e}_\lambda
\end{aligned} \tag{31}$$

2.3 Gravity gradient kernels

Depending on application, the integral can be practical to evaluate either in Cartesian or in spherical coordinates. The tensor Green functions describing the gravity gradients in Earth-centered reference frame is (e.g. Martinec (2014))

$$\nabla\nabla G(\mathbf{r}, \mathbf{r}') = -\frac{1}{|\mathbf{r} - \mathbf{r}'|^3} \left[\mathbf{I} - \frac{3\,(\mathbf{r} - \mathbf{r}') \otimes (\mathbf{r} - \mathbf{r}')}{|\mathbf{r} - \mathbf{r}'|^2} \right]. \tag{32}$$

The comparison of model results with the GOCE data requires the coordinate transformation according to the traditional in geophysics sign convention for the gravity gradients. In particular, the radial gravity gradient anomaly is assumed positive for a positive mass anomaly in the local coordinate frame (x-north, y-west and z-up).

The zero-order approximation for the forward problem (Wild-Pfeiffer, 2008) which is equivalent to the sum of point masses is found sufficiently accurate for the geometry of our problem. The geocentric radius for each layer R is the is referenced to the center of mass of each volume element. Using eq. (32) together with eqs (13)-(14), the Green's function for the radial gravity gradient can be written

$$G_{rr} = \frac{\partial^2 G}{\partial r^2} = -\frac{1}{|\mathbf{r} - \mathbf{r}'|^3} + \frac{3\left(r - r'\cos\psi\right)^2}{|\mathbf{r} - \mathbf{r}'|^5}. \tag{33}$$

The Green function corresponding to the gravity anomaly on the sphere is

$$G_r = \frac{r - r'\cos\psi}{|\mathbf{r} - \mathbf{r}'|^3}. \tag{34}$$

The integral eq. (6) written in the discrete matrix form for the gravity gradient tensor is

$$\mathbf{d} = \mathbf{G}\mathbf{m} \tag{35}$$

where $\mathbf{d}$ is the data vector, $\mathbf{G}$ is the system matrix and $\mathbf{m}$ is the density vector.

The conversion of gravity gradient tensor in the local Cartesian system spherical coordinates (LNOF) to the x-, y-, z- tensor components in global Cartesian system (ECEF) can be performed by tensor rotation:

$$\mathbf{d}' = \mathbf{Q}^T \mathbf{d} \mathbf{Q}, \tag{36}$$

where $\mathbf{Q}(\phi, \theta)$ is the transformation matrix (Bouman et al., 2013).

2.4 Solution of the inverse problem

We assume a linear model that connects data and model parameters in the form of eq. (35). The Gaussian probability distribution for the data can be written

$$p(\mathbf{d}) \propto \exp\left(-\frac{1}{2\sigma_d^2}\left(\mathbf{G}\mathbf{m} - \mathbf{d}\right)^T \mathbf{\Sigma}_d^{-1}\left(\mathbf{G}\mathbf{m} - \mathbf{d}\right)\right) \tag{37}$$

with data correlation function $\mathbf{\Sigma}_d$ and variance σ_d^2.

We apply following *a priori* constraints as spatial weighting function (Li & Oldenburg, 1996; Zhdanov et al., 2011)

$$\mathbf{m}_w = \mathbf{W}\mathbf{m}. \tag{38}$$

The Gaussian probability distribution for the model parameters can be expressed in the form

$$p(\mathbf{m}) \propto \exp\left(-\frac{1}{2}\left(\mathbf{m} - \mathbf{m}_0\right)^T \mathbf{W}^T \mathbf{C}_w^{-1} \mathbf{W}\left(\mathbf{m} - \mathbf{m}_0\right)\right) \tag{39}$$

C_w^{-1} is the covariance of the weighted parameters and $\mathbf{m}_0$ is the prior density model.

We assume that the covariance of weighted parameters is related to the density covariance as

$$\mathbf{C}_w = \alpha^{-1}\mathbf{C}_m = \alpha^{-1}\sigma_m^2 \mathbf{\Sigma}_m \tag{40}$$

where α^{-1} is a coefficient approximately equal to the mean of the squared diagonal elements of the weighting matrix $\mathbf{W}$

$$\alpha^{-1} \approx \frac{1}{N}\sum_{i=1}^{N} w_i^2, \tag{41}$$

$\mathbf{\Sigma}_m$ is the correlation function, σ_m^2 is the variance.

The joint posterior probability can be written in the form

$$p(\mathbf{m}|\mathbf{d}) \propto \exp\Big(- \Phi(\mathbf{m})\Big) \tag{42}$$

with

$$2\Phi(\mathbf{m}) = \sigma_d^{-2}\big(\mathbf{Gm}-\mathbf{d}\big)^T\mathbf{\Sigma}_d^{-2}\big(\mathbf{Gm}-\mathbf{d}\big) + \alpha\sigma_m^{-2}\big(\mathbf{m}-\mathbf{m}_0\big)^T\mathbf{W}^T\mathbf{\Sigma}_m^{-1}\mathbf{W}\big(\mathbf{m}-\mathbf{m}_0\big). \tag{43}$$

The mean and the covariance function that maximize the posterior probability can be written as solution of a least-squares problem. The solution corresponding to the inversion in data space (Tarantola, 2004):

$$\begin{aligned} \Delta\mathbf{m}_w &= \mathbf{G}_w^\dagger\left[\mathbf{G}_w\mathbf{G}_w^\dagger + \alpha\mathbf{I}_d\right]^{-1}\delta\mathbf{d}, && (44)\\ \tilde{\mathbf{\Sigma}}_m &= \mathbf{\Sigma}_m - \mathbf{G}_w^\dagger\left[\mathbf{G}_w\mathbf{G}_w^\dagger + \alpha\mathbf{I}_d\right]^{-1}\mathbf{G}_w\mathbf{\Sigma}_m && (45) \end{aligned}$$

where $\Delta\mathbf{m}_w = \mathbf{W}\big(\mathbf{m}-\mathbf{m}_0\big)$ are weighted model parameters, $\mathbf{G}_w = \mathbf{G}\mathbf{W}^{-1} = \mathbf{W}^{-1}\mathbf{G}^T$ is the weighted kernel, $\mathbf{I}_d$ is the identity matrix with the size equal to the number of data points, the data residuals denoted as $\Delta\mathbf{d} = \mathbf{d}-\mathbf{G}\mathbf{m}_0$ and the adjoint weighted kernel $\mathbf{G}_w^\dagger$ defined as

$$\mathbf{G}^\dagger = \frac{\sigma_m^2}{\sigma_d^2}\mathbf{\Sigma}_m\mathbf{G}_w^T\mathbf{\Sigma}_d^{-1}. \tag{46}$$

The solution can also be written in an alternative form in the case of inversion in the model space:

$$\begin{aligned} \Delta\mathbf{m}_w &= \tilde{\mathbf{G}}_w^\dagger\delta\mathbf{d}, && (47)\\ \tilde{\mathbf{\Sigma}}_m &= \mathbf{\Sigma}_m\left[\mathbf{G}_w^\dagger\mathbf{G}_w + \alpha\mathbf{I}_m\right]^{-1} && (48) \end{aligned}$$

where $\tilde{\mathbf{G}}_w^\dagger = \frac{\sigma_m^2}{\sigma_d^2}\tilde{\mathbf{\Sigma}}_m\mathbf{G}_w^T\mathbf{\Sigma}_d^{-1}$ and $\mathbf{I}_m$ is the identity matrix with the size equal to the number of model parameters.

The ensemble of random realization corresponding to the posterior probability density function can be obtained using the Cholesky decomposition of the posterior covariance matrix $\mathbf{C}_m$

$$\mathbf{m}_{ens} = \Delta\mathbf{m} + \mathbf{L}^T\xi. \tag{49}$$

Here, $\Delta\mathbf{m}$ is the solution for the mean density distribution, ξ is a vector of mutually independent random numbers with zero mean and unit variance and $\mathbf{L}$ is the matrix of Cholesky factors such as $\mathbf{C}_m = \mathbf{L}^T\mathbf{L}$.

2.5 Data and model covariance matrices

Assuming a stationary Gaussian random process, the covariance matrix $\mathbf{K}$ is related to the variogram $\gamma(h)$ estimated at the distance h between a pair of points as

$$\mathbf{K}(h) = \mathbf{K}(0) - \gamma(h) = \sigma_d^2 - \gamma(h), \tag{50}$$

where σ_d^2 is the data variance. The variogram, estimated using N grid points at the spherical distance h, can be expressed as

$$\gamma(h) = \frac{1}{2N(h)} \sum_{i=1}^{N(h)} \left(\delta v(x_i + h) - \delta v(x_i)\right)^2, \tag{51}$$

where $\delta v(x)$ is the parameter variation with respect to the mean value.

The uncertainty of the Moho depth dominates the uncertainty of the residual gravity signal. We neglect other factors might contribute to the uncertainty, and obtain the data covariance matrix using the covariance for the Moho depth $\mathbf{C}_s$ and the surface Green function $\mathbf{G}_s$ at the regional average radial distance

$$\tilde{\mathbf{C}}_d = \mathbf{G}_s \mathbf{C}_s \mathbf{G}_s^T. \tag{52}$$

The normalization is required to ensure that patches with the same spherical surface area have the same probability:

$$\mathbf{C}_d = \frac{1}{\cos\phi} \tilde{\mathbf{C}}_d. \tag{53}$$

The prior information about the length scale and spatial variability of the density field can be incorporated using the covariance matrix. For the model parameter covariance inside the sphere, we assume the statistical model by Kolyukhin and Minakov (2020):

$$\mathbf{C}_m = \sigma_m^2 \mathbf{\Sigma}_\Omega(\phi, \lambda) \mathbf{\Sigma}_r(r), \tag{54}$$

where σ_m^2 is the model variance, $\mathbf{\Sigma}_\Omega(\phi, \lambda)$ and $\mathbf{\Sigma}_r(r)$ are the angular and the radial correlation functions, respectively. The correlation functions can be obtained using the variogram method. There are a number of functions that can be used to approximate empirical variogram (Terdik et al., 2015; Lantuéjoul et al., 2019). In this work, the angular covariance is approximated using the inverse distance model (Terdik et al., 2015).

$$\mathbf{\Sigma}_\Omega(\phi, \lambda) = \left(1 + a^2 - 2a\cos\psi\right)^{-1/2}. \tag{55}$$

Here, the correlation length depends on the parameter $|a| < 1$.

The variogram in the radial direction is approximated using an exponential-type covariance (Monin & Yaglom, 1975) (their eq. 11.20)

$$\mathbf{\Sigma}_r(r) = \exp(-b_1|\mathbf{r}|)\cos b_2|\mathbf{r}|, \tag{56}$$

with the correlation length defined by the parameters b_1 and b_2. The sensitivity of S-wave velocities and density to temperature changes, inferred from empirical data, can be used to obtain the model constraints in terms of spatial correlations.

2.6 Spatial weighting and depth resolution

The function $\mathbf{W}$ acts as a stabilizing functional for the inverse problem and provides depth weighting to each parameter according its contribution to the data points used in the inversion (Zhdanov, 2015). The integrated sensitivity of the data at the observation plane S to variation of the model parameter k can be expressed as

$$\mathbf{W}^T\mathbf{W} = \operatorname{diag}\left(\frac{||\delta \mathbf{d}||}{\delta m_k}\right) = \operatorname{diag}\left(\sqrt{\iint_S G_k^2 dS}\right). \tag{57}$$

The shape of the averaged gravity gradient kernel at a point centered at the origin of coordinate eq. (32) is azimuthally symmetric. For analytical demonstration of the form of the weighting function, it is convenient to perform integration in cylindrical coordinates:

$$\mathbf{W}^T\mathbf{W} = \operatorname{diag}\left(\sqrt{\int_0^{2\pi} d\phi \int_0^{\infty} G_k^2 r dr}\right). \tag{58}$$

Using the expression for the eigenvalue of the gravity gradient tensor corresponding to a point mass (Pedersen & Rasmussen, 1990), the integral in eq. (58) can be written as

$$2\pi \int_0^{\infty} G_{ik}^2 r dr = 2\pi \int_0^{\infty} \frac{2r}{(r^2+z^2)^3} dr = -\frac{\pi}{(r^2+z^2)^2}\bigg|_0^{\infty} = \frac{\pi}{z^4} \tag{59}$$

where $r = \sqrt{x^2+y^2}$ is the radial distance from the origin to the observation point. After the square root is applied twice, the model weighting coefficients become proportional to the inverse distance from the observation point to the point mass:

$$w_i \propto 1/z_i. \tag{60}$$

Such spatial weighting suppresses model variation in the shallow part of the model (with respect to the prior model) and enhances model variation in the deeper part of the model.

To better understand the density imaging using satellite gradiometry data, it is useful to analyze properties of the integrated gravity gradient kernel. The principles of potential field imaging (Zhdanov et al., 2011) can be illustrated on the example of vertical gradient U_{zz}. The integrated kernel is directly related to the migration density field if the data represent a boxcar function:

$$K_{zz} = \int_0^{2\pi} d\phi \int_0^{r_0} \frac{r}{(r^2+z^2)^{3/2}} \left(\frac{3z^2}{r^2+z^2} - 1\right) dr. \tag{61}$$

This definite integral equals to

$$K_{zz} = \frac{2\pi r_0^2}{(r_0^2+z^2)^{3/2}}. \tag{62}$$

The maximum of the kernel is located at the surface before the weights in eq. (60) are applied:

$$K_{zz} = \frac{2\sqrt{\pi} r_0^2 z^2}{(r_0^2 + z^2)^{3/2}}. \tag{63}$$

The kernel has a larger geometrical spreading with depth for wider gravity gradient anomalies. The maximum of this weighted kernel and corresponding maximum of the migration density field can be found at the extreme point:

$$\frac{\partial K_{zz}}{\partial z} = \frac{2\sqrt{\pi} r_0^2 z \left(2r_0^2 - z^2\right)}{\left(r_0^2 + z^2\right)^{5/2}} = 0. \tag{64}$$

From where, the predicted maximum of imaged density field is related to the radius of the integration region as

$$z = \sqrt{2} r_0. \tag{65}$$

For the 2D case, using analytical integration in the complex plane, Zhdanov (2015) has shown that the gravity migration density distribution has a maximum at the location of the point mass. Similarly, it can also be shown numerically for the case of 3D geometry.

2.7 Numerical implementation of the gravity gradient inversion

A least squares solution in the form of eq. (44) can be obtained using an iterative solution technique (Liang et al., 2014; Barnoud et al., 2016) such as the method of conjugate gradients and LSQR (Paige & Saunders, 1982) . For three dimensional problems, the system matrix quickly grows and this approach becomes computationally challenging. Alternatively, we can use the formulation of the inversion in the data space eq. (44), (45). In this case, the matrix to be inverted is of the data size and can be performed using the singular value decomposition (Chasseriau & Chouteau, 2003). Moreover, assuming that the data are uncorrelated, we can modify the probability function of model parameters by incorporating new data, such as additional measurements, or combine different gravity gradient components. Applied successively to each data point, this method does not require inversion of large matrix, and, therefore, can be numerically efficient. The corresponding least-squares solution is based on eqs (44),(45) (see Tarantola (2004)). Using our notation it can be written as

$$\mathbf{m}_w^{(k+1)} = \mathbf{m}_w^{(k)} + H^{-1}\mathbf{q}\delta d_k \tag{66}$$

$$\mathbf{C}_m^{(k+1)} = \mathbf{C}_m^{(k)} - H^{-1}\mathbf{q}\mathbf{q}^T \tag{67}$$

$$\delta d_k = d_k - \mathbf{G}_k \mathbf{W}^{-1}\mathbf{m}_w^{(k)} \tag{68}$$

$$\mathbf{q} = \sigma_d^{-1}\mathbf{C}_m^{(k)}\mathbf{G}_k\mathbf{W}^{-1} \tag{69}$$

$$H = \alpha + \mathbf{G}_k\mathbf{W}^{-1}\mathbf{q} \tag{70}$$

The k index denotes current data point with the mean d_k and variance σ_d. $\mathbf{G}_k$ is the system matrix eq. (35) with the number of rows corresponding to the number of data components (a row vector for single-component data). The memory requirements can be substantially reduced by noticing the local nature of gravity gradient kernels. Therefore, only significant $\mathbf{G}_k$ elements can be selected. We found that model parameters beyond 600-700 km distance from the observation point have a very small contribution to the data, and, thus, corresponding matrix elements of $\mathbf{G}_k$ and $\mathbf{C}_m$ can be ignored without a substantial change of the solution. The vector $\mathbf{q}$ is analogous to the adjoint operator $\mathbf{G}^\dagger$ (eq. (46)). The matrix H reduces to the scalar for single-component data H (or a small square matrix with the size of the number of data components). Note that the mean weighted density $\mathbf{m}_w^{(k)}$ and the covariance matrix $\mathbf{C}_m^{(k)}$ are updated at each iteration k. The final density model $\mathbf{m} = \mathbf{W}^{-1}\mathbf{m}_w$ is obtained after the last data point

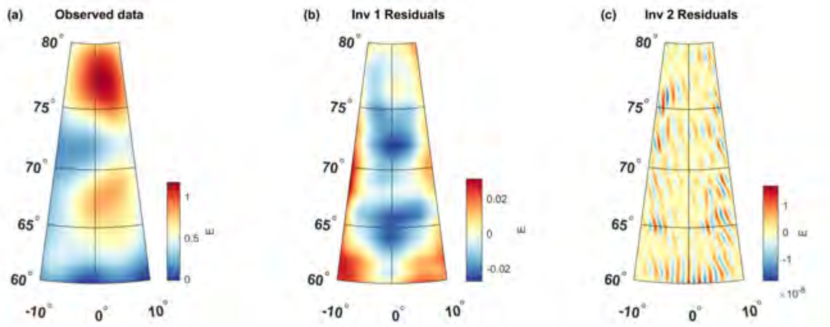

Figure 4. Reconstructed synthetic data using a spherical random density model. (a) synthetic input data (radial gravity gradient); (b) the data residuals obtained using the LSQR damped least squares inversion method; (c) the data residuals obtained using the recursive least squares inversion method with the constrained covariance model.

has been assimilated. Equation (66) allows for a rapid density imaging method similar to the potential field migration suggested by Zhdanov et al. (2011).

2.8 Synthetic tests

The 3D synthetic density model represents a spherical shell model with the lateral extent of 20°X20° and the bottom at the top mantle transition zone (410 km depth). The model is parameterized using 20 layers comprised of spherical prisms with a 0.5-degree resolution. We simulate the density anomalies in the model as a Gaussian random field with zero mean and covariance determined by eqs (54)-(55). The description of the numerical method for the random field simulation inside the sphere can be found in Meschede and Romanowicz (2015) and Kolyukhin and Minakov (2020). The parameters defining the covariance model were selected according to the empirical correlation functions (Fig. 10) estimated using the seismic tomography model for the northeast Atlantic region by Rickers et al. (2013); Fichtner et al. (2018) . We calculate the radial gravity gradient signal (Fig. 4a) corresponding to the random density model (Fig. 5a) using eqs (6) and (33). The density distribution was reconstructed using the two methods described in section 2.7.

The first modeling approach we have used is the LSQR method with diagonal covariance matrices ($\sigma_d = \pm 10\,\mathrm{s}^{-1}$, $\sigma_m = \pm 10\,\mathrm{kgm}^{-3}$) and the zero prior mean density anomaly. An optimal damping parameter was found based on the standard L-curve criterion (Aster et al., 2018). The data residuals and reconstructed model are shown in Fig. 4b and Fig. 5b. The inversion recovers the lateral position, depth to the center of mass and average intensity of density anomalies in the model. The depth smearing limits the resolution of fine structures in the model.

The second method we have applied is the recursive least squares inversion in the data space with the full model covariance matrix and the diagonal data covariance matrix. The simulations results are in Fig. 4c and Fig. 5c. The constraints on spatial correlations in the model allows recovering not only average position (center of mass) of the density anomalies by also their correct aspect ratio. The spatial correlation controls the shape, relative strength and depth of individual density anomalies.

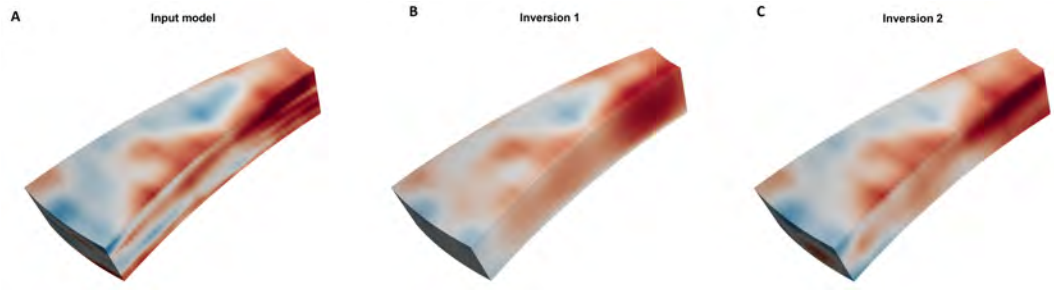

Figure 5. Reconstructed synthetic spherical random density model. (a) synthetic input model. The covariance model is defined by eqs (55),(56) with $a = 0.94$, $b_1 = 0.03$, and $b_2 = 0.1$. (b) the model obtained using the LSQR damped least squares inversion method. (c) the model obtained using the recursive least squares inversion method with the constrained covariance model.

3 Results

3.1 Gravity and gravity gradient signals of lithospheric layers

We assume that the total gravity signal in the North Atlantic consists of the following main components: 1) topography (elevation and bathymetry) and the associated Bouguer correction; 2) ice thickness variation; 3) sedimentary thickness variation, constrained by multichannel seismic data; 4) crustal thickness and density variations, constrained by wide-angle seismic data; 5) lithospheric thickness variation due to stretching and subsequent cooling, constrained by crustal age grid (Fig. 2); and 6) density variation in the upper mantle. The long-wavelength signal due to lower-mantle density variations was neglected since it is found to be small in gravity gradients compared to this signal in the geoid and the gravity anomaly field (see Fig. 3).

The topography and bathymetry data were extracted from the international GEBCO2020 bathymetry and topography data including the ice thickness model over Greenland `https://www.gebco.net` (Fig. 2). The topography/Bouguer correction is performed using the reduction density of 2850 $\mathrm{kg\,m^{-3}}$. The density of ice is assumed 970 $\mathrm{kg\,m^{-3}}$. The global sediment thickness grid is combined using the marine sedimentary thickness by Straume et al. (2019) and the CRUST1.0 sediment thickness on land (Laske et al., 2013; Szwillus et al., 2019). Regional sedimentary thickness and crustal thickness data are based on the seismic reflection and refraction database compiled during NAGTEC project `http://www.nagtec.org` (Funck et al., 2017) . The assumed sediment density is 2400 $\mathrm{kg\,m^{-3}}$. The average density of crystalline crust follows the results of statistical interpolation by Szwillus et al. (2019). The density variation within the crustal layer is found to have a second-order effect compare to the crustal thickness variation. The lithospheric cooling correction (Fig. 7c,d) is computed using a pure shear lithospheric extension model (McKenzie, 1978) and the ocean age grid (Gaina, Nasuti, et al., 2017).

We have estimated spherical harmonic coefficients for each crustal density layer using global spherical harmonic analysis (Sneeuw, 1994; Wieczorek, 2007). Then, we calculated the gravitational potential (Stokes) coefficients from which the gravitational potential and its functionals can be obtained (Novák & Grafarend, 2006). The residual gravity and gravity gradient anomalies correspond to the observed data after the effects of each individual crustal layers has been subtracted (Fig. 8).

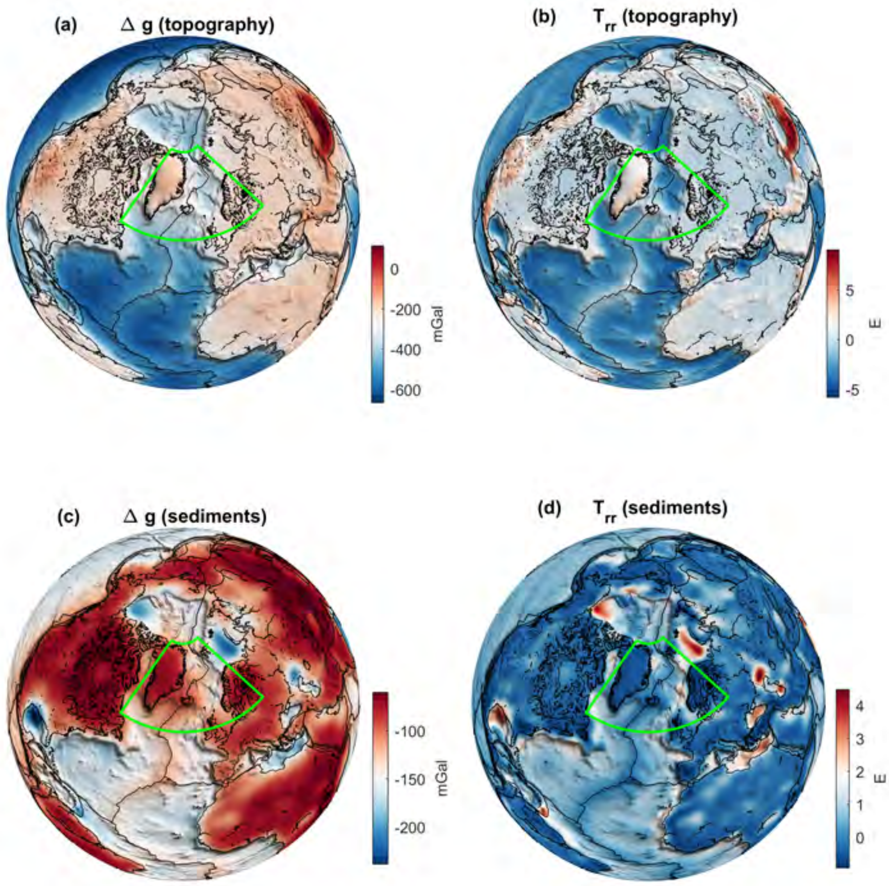

Figure 6. Gravity and radial gravity gradient anomaly due to the variation of topography (a,b) and sediment thickness (c,d) at the height of 220 km. The sector indicates the northeast Atlantic study region.

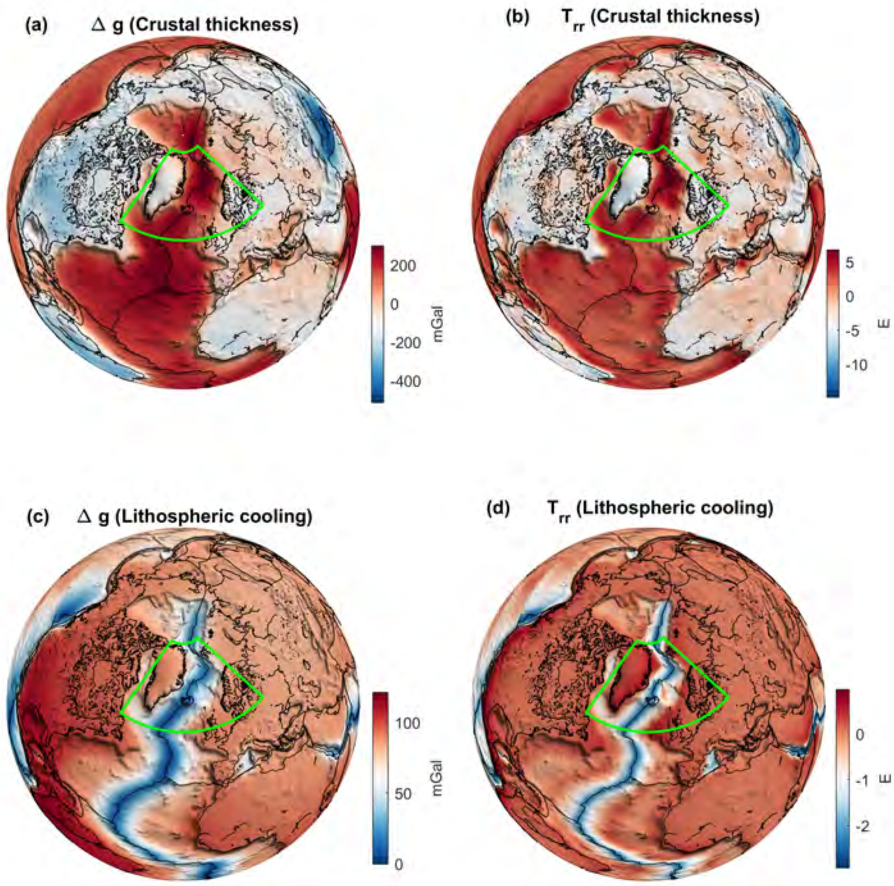

Figure 7. Gravity and radial gravity gradient anomaly due to the variation of crustal thickness (a,b) and oceanic crustal age (c,d) at the height of 220 km. The sector indicates the northeast Atlantic study region.

3.2 Residual gravity and gravity gradient signal

The goal of the following analysis is to extract from the observed gravity data the gravity signal corresponding to the 3D heterogeneous density structure of the lithosphere and sub-lithospheric upper mantle. We subtract from the observed data in Fig. 1 the signal of the crust including the topography correction and the thermal density signal due to lithospheric cooling (Fig. 7).

The residual gravity and radial gravity gradient anomalies emphasize the effects of dense and cold continental roots and low-density regions adjacent to the Iceland hotspot region. The gravity effect of localized lithospheric density anomalies is more pronounced in residual gravity gradient anomalies than in the total field. The range of variation is from about -100 mGal to 75 mGal and ±2-3 E, for the gravity and the gravity gradient, respectively.

The obtained residual gravity gradients (Fig. 8) can be linked to the density variation unaccounted by the 3D reference model. The amplitude values of the residual gradients ($\pm 2 - 3\,\mathrm{E}$) is about twice of the observed gradients, and the crustal correction constitutes about 2/3 of the total signal. A rough estimate of the gravity gradient signal associated with a 100-km size spherical density anomaly due to a temperature change of 100 K located in a middle upper mantle would correspond to about 1 E.

The interpretation of the residual signal is most transparent in the case of the radial gravity gradient (Fig. 8). The lithospheric and upper mantle signal is more pronounced in the residual gravity gradient signal (Fig. 8b,d) than in the residual gravity anomalies (Fig. 8a,c). The residual signal shows a correlation with the upper mantle seismic velocity anomalies in the global tomography model by Schaeffer and Lebedev (2013). In particular, at the depth of 80 km (Fig. 8d) in the oceanic, both to the north and south of Iceland, and within cratonic regions. The negative residual signal at the east Greenland margin, the south Norway region and northern British Isles implies a low-density lithosphere at depth. The Fennoscadian craton appears colder and thicker compared to the Greenland lithosphere in both seismic tomography model and gravity data. Note that the observed data in Figs 1 and 3 show anti-correlation with the seismic anomalies (see also Sebera et al. (2017)).

3.3 Statistical characterization of input data and prior information

The non-uniqueness of the inverse problem can be addressed using various approaches to incorporate prior information. In our case, the largest uncertainty in the data (residual gravity gradient signal) arises from the uncertainty of the crustal thickness due to non-homogeneous coverage of wide-angle seismic data. This prior information is incorporated in the inversion using the data covariance matrix $\mathbf{C}_d$. Assuming a linear model between data and model parameters, the variance of crustal thickness can be translated to the data variance (Fig. 9) using eq. (52). We find the probability distribution for the crustal thickness following the geostatistical method described in Szwillus et al. (2019). Since the full original dataset is not available, we extracted the actual Moho depth values from corresponding published grids (Funck et al., 2017; Mooney, 2015; Szwillus et al., 2019) along the profile coordinates with a step of 10 km, assuming that the values at the data locations have not been biased by the interpolation in the regional grid. Then, we applied a spherical kriging interpolation to the obtained dataset.

The data covariance matrix $\mathbf{C}_d$ was obtained from the Moho variance grid using eq. (52) and the gravity gradient kernel eq. (33). For simplicity, we consider only diagonal elements of this matrix and imply that the data points are independent. This assumption is not generally required but allows for an efficient numerical implementation. The diagonal elements of $\mathbf{C}_d^{-1/2}$ (standard deviation) shown in Fig. 9 imply the largest variance over southwestern Greenland ($\sigma_d^{1/2} > 1$ Eotvos). The passive margin of Nor-

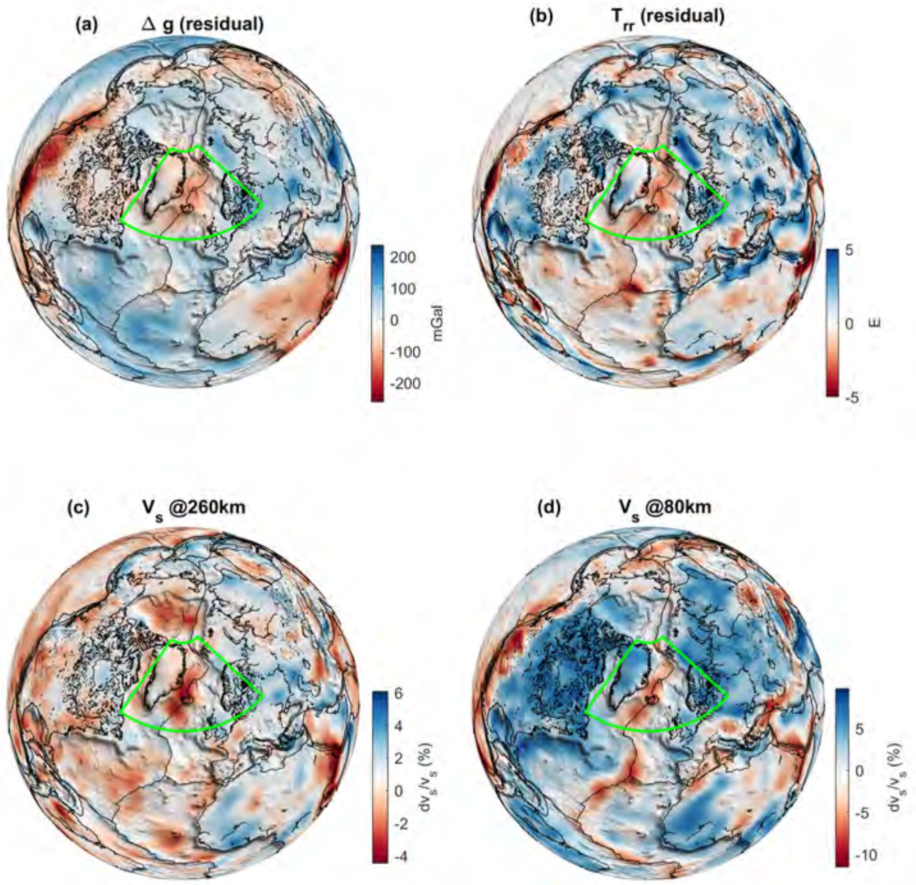

Figure 8. The residual gravity and radial gravity gradient (a,b) and seismic shear velocity perturbation at the depth of 260 km (c) and 80 km (d) in the global tomography model by Schaeffer and Lebedev (2013). The sector indicates the northeast Atlantic study region.

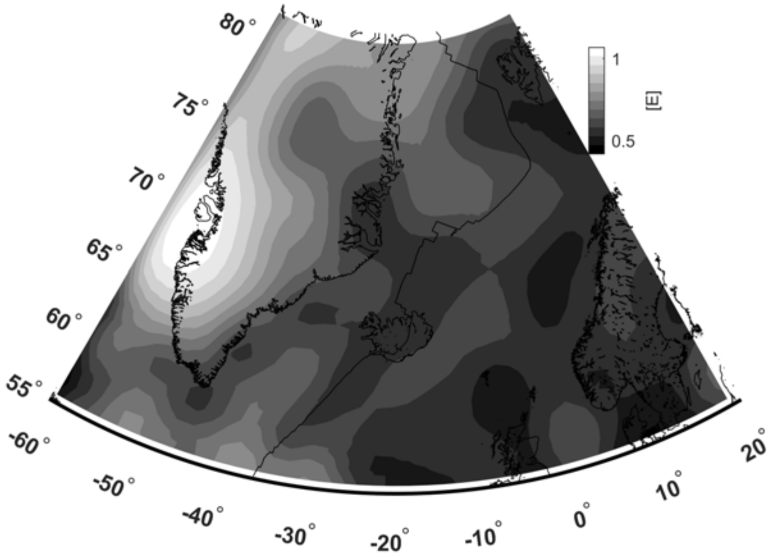

Figure 9. Data uncertainty (square root of the diagonal data covariance matrix $\mathbf{C}_d$)

way is densely covered by seismic profiles and has small data uncertainty ($\sigma_d^{1/2} < 0.5$ Eotvos).

The model covariance matrix $\mathbf{C}_m$ can be obtained using the variogram method described in section 2.5. We applied this method to the seismic shear velocity variation in the regional tomography model by Rickers et al. (2013); Fichtner et al. (2018) which has a better spatial resolution compare to global models. We assume that the spatial correlations of seismic velocity and density anomalies are similar. Fig. 10 shows the radial correlation function ($\mathbf{\Sigma}_r$), estimated for a bin size of 20, 30 and 40 points, at the depth of 50-410 km, after the 1D mean has been removed. The estimated correlation becomes negative beyond a radial distance of about 150 km. This type of spatial variation can be approximated in the analytic form by a combination of exponential and cosine functions (Monin & Yaglom, 1975). We have also estimated the correlation depending on the spherical distance up to 0.5 rad (or about 3000 km) at four different depth intervals between 65 km and 265 km depth. The angular correlation function ($\mathbf{\Sigma}_\Omega$) can be represented by the inverse distance model (Lantuéjoul et al., 2019) with the coefficient a between 0.9 and 0.99 depending on the depth.

3.4 Inversion of residual gravity gradients

The density model was parameterized as a spherical shell with a lateral grid resolution of 50-70 km and the depth resolution of about 20 km. The single-component inversion was performed using the residual radial gravity gradient signal (T_{rr}) shown in Fig. 11. The range of the signal is ±3 Eotvos. In the inversion setup, we assume a zero density variation as a prior model. The predicted mean density model is presented for the depth of 150 km (Fig. 13).

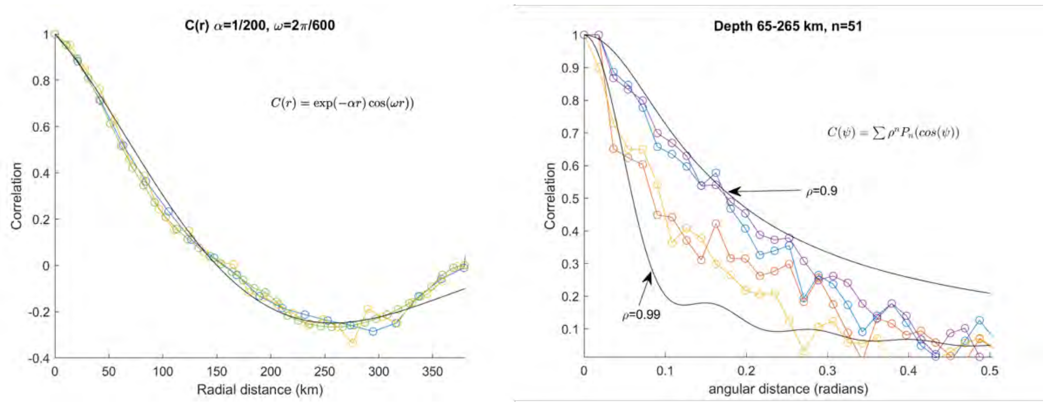

Figure 10. Empirical radial (a) and angular (b) correlation functions estimated using the seismic S-wave tomography model and the variogram method. (a) the color indicates various bin sizes (20, 30 and 40 data points). (b) the color indicates the correlation function estimated at four different depth intervals (65-115 km, 115-165 km, 165-210 km and 210-265 km); the bin size is 30 points.

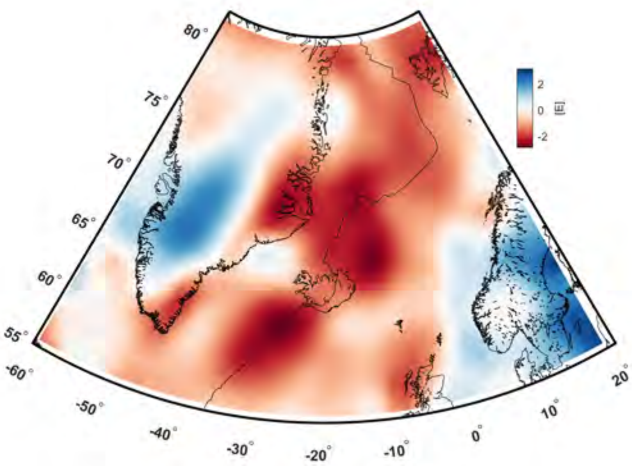

Figure 11. Residual gravity gradient anomalies ($\mathbf{T}_{rr}$). The coastlines and mid-Atlantic ridge axis are shown.

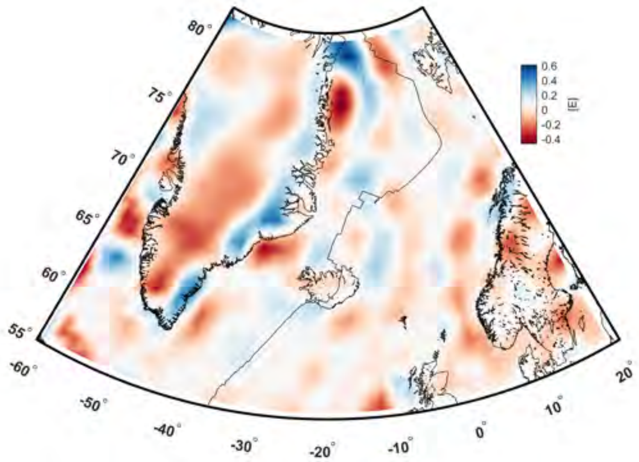

Figure 12. The misfit of predicted gravity gradient signal ($\mathbf{T}_{rr}$) based on the final density model. The coastlines and mid-Atlantic ridge axis are shown.

The calculated data misfit shows no systematic pattern (Fig. 12). The range of the misfit is about ± 0.5 Eotvos which is generally within the data uncertainty $2\sigma_d^{1/2}$ (cf. Fig. 9).

The general pattern of the density perturbation reflects the distribution of residual anomalies in Fig. 13. The predicted negative density anomalies in the upper mantle correlate with a wider region along mid-ocean ridges where seamount volcanism may have been active since the Oligocene (ca 30 Ma). In addition, the thinned continental crust of Rockall Plateau, where older seamounts were emplaced (ca. 50-60 Ma), is underlain by a low-density upper mantle (Fig. 13). The most intense negative mantle density anomaly (about -40 kg m^3) at the west Greenland margin corresponds to the early Cenozoic location of the Iceland hotspot (Torsvik et al., 2015). The Greenland-Iceland-Faeroe ridge is underlain by a positive density anomaly in the shallow lithosphere. The negative density anomalies are observed underneath the Caledonian deformation front in northern British Isles and southern Norway. The mass deficit under the central-east Greenland margin and across Greenland is expressed in the density model at middle upper mantle depths.

The comparison with regional high-resolution seismic tomography model (V_{SH}) by Rickers et al. (2013); Fichtner et al. (2018), shown at the same depth, indicate a similar correlated pattern of positive and negative anomalies. The negative anomalies are located along the mid-Atlantic ridge, and to a lesser extent under northern British Isles and the Norwegian margin. The positive anomalies are below the cratonic parts of Greenland and Fennoscandia. The dissimilarities between the tomography and gravity models at a particular depth can be partly related to the non-uniqueness of the inverse gravity problem such as along the Iceland-Faeroe Ridge and at the west Greenland margin (Fig. 13 and Fig. 14). A more detailed discussion on the predicted mantle density variation with its relation to crustal structure and seismic velocities along three regional transects follows in the next chapter.

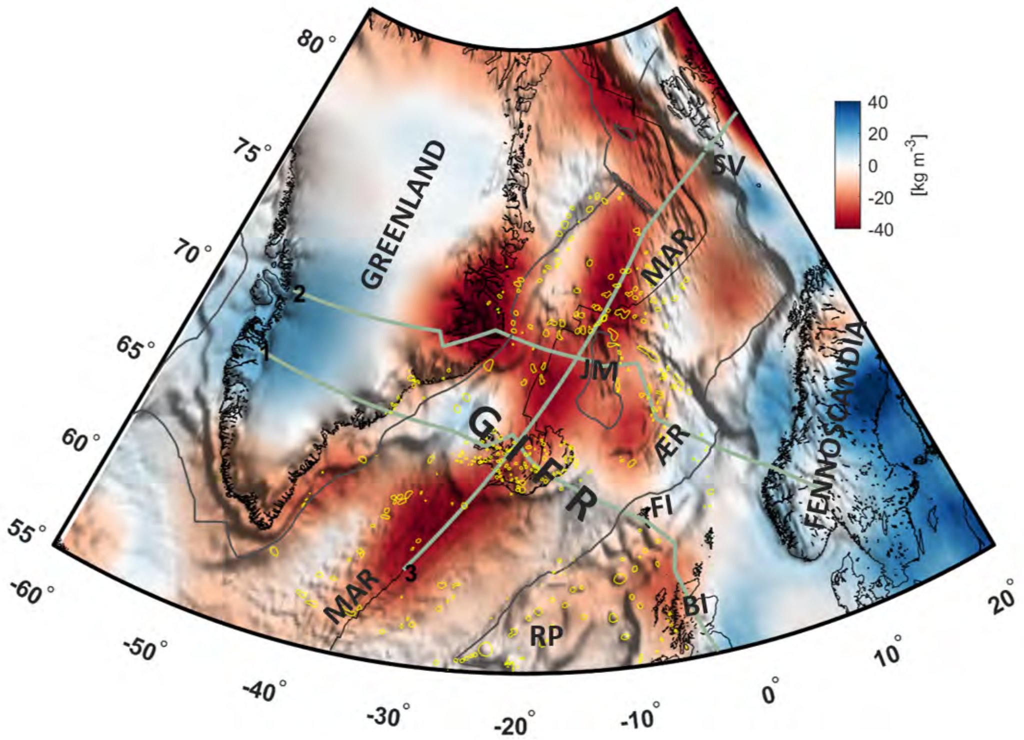

Figure 13. Density anomalies at 150-km depth based on inversion of the residual radial gravity gradient field. The grey lines indicate the location of the model transects. The volcanic centers and seamount-like features identified by Gaina, Blischke, et al. (2017) are indicated by yellow contours. The coastlines, continent-ocean boundaries and the mid-Atlantic ridge axis are shown. ÆR - Ægir Ridge; BI - British Isles; FI - Faeroe Islands; GIFR - Greenland-Iceland-Faeroe Ridge; JM - Jan Mayen Microcontinent; MAR - Mid-Atlantic Ridge; RP - Rockall Plateau; SV - Svalbard.

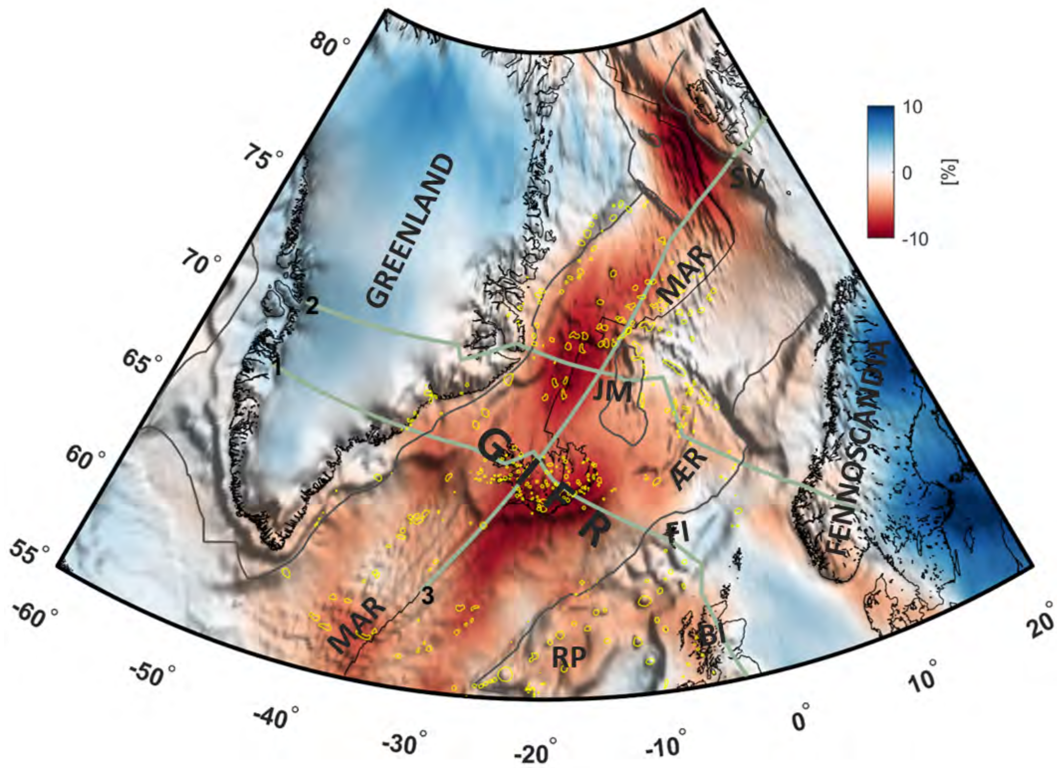

Figure 14. Velocity anomalies at 150-km depth based on tomography model by Rickers et al. (2013); Fichtner et al. (2018). The grey lines indicate the location of the model transects. The volcanic centers and seamount-like features identified by Gaina, Blischke, et al. (2017) are indicated by yellow contours. The coastlines, continent-ocean boundaries and the mid-Atlantic ridge axis are shown. ÆR - Ægir Ridge; BI - British Isles; FI - Faeroe Islands; GIFR - Greenland-Iceland-Faeroe Ridge; JM - Jan Mayen Microcontinent; MAR - Mid-Atlantic Ridge; RP - Rockall Plateau; SV - Svalbard.

4 Discussion

4.1 Mantle density and seismic velocity anomalies along lithospheric transects

Several regional seismic tomography studies have shown an irregular-shape low-velocity seismic anomaly in the upper mantle in the northeast Atlantic region resolved in both S-wave (Pilidou et al., 2005; Legendre et al., 2012; Rickers et al., 2013; Fichtner et al., 2018; Lebedev et al., 2018) (Fig. 14) and P-wave velocity models (Bijwaard & Spakman, 1999; Jakovlev et al., 2012; Hosseini et al., 2020), and can be linked to the Cenozoic Iceland plume activity. The anti-correlation of the seismic velocity and long-wavelength gravity anomalies have previously been discussed by Jones et al. (2002); Rickers et al. (2013); Sebera et al. (2017). Our results are in agreement with their conclusion that the long-wavelength positive gravity anomalies (and corresponding dynamic topography) are associated with the low-density material in the asthenosphere.

The regional S-wave tomography model by Rickers et al. (2013); Fichtner et al. (2018) is based on full-waveform inversion of surface and body waves, and has previously been used to infer geodynamic processes in the northeast Atlantic region (Schoonman et al., 2017). Here, we compare the S-wave velocity anomalies in the tomography model with our density model (Fig. 13) along three lithospheric-scale transects. Each synthetic transect is characterized by good constraints on crustal structure based on controlled-source seismic data. The synthetic transects, whenever it is possible, follow available seismic lines and illuminate key tectonic features of the study area. The transects are shown for the upper 300 km, the region where most of density variation resides.

4.1.1 Profile 1

The west-east Profile 1 (Fig. 15) runs across Greenland (0-750 km), along the Greenland-Iceland-Faeroe Ridge (GIFR) (750-2100 km) and northern British Isles (2100-3000 km) where it intersects the main Caledonian suture zone (Barton, 1992). The profile crosses the thick and cold Greenland craton where crustal thickness is mainly constrained by receiver function data (Dahl-Jensen et al., 2003). Further east, the profile runs along the western portion of GIFR with thick high-velocity igneous or transitional crust (Korenaga et al., 2000; Yuan et al., 2020). The crustal thickness of the mainly volcanic Iceland Plateau reaches about 40 km, as it was estimated from the receiver function analyses (Kumar et al., 2007) and wide-angle profiles by Darbyshire et al. (1998) and Staples et al. (1997). In a regional context, Iceland is part of GIFR which represents a complex region of excessive magmatic crustal accretion due to overlapping rift systems, interlinked rifts and transform zones with a variable uplift and subsidence history (Hjartarson et al., 2017). In such excessively magmatic regions, high-density ultramafic rocks can be emplaced at or above Moho (Richards et al., 2013; Funck et al., 2017), and significantly decrease the density contrast at the crust-mantle interface. The P-wave velocity and density structure along the eastern part of GIFR is apparently similar to the western part; although, the velocity model might be poorly resolved due to short source-receiver offsets.

The lithospheric density images derived using the gravity gradient inversion provide complementary information to seismological data. The thin extended continental crust within the Faeroe Basin (Raum et al., 2005) is underlain by slightly denser upper mantle compared to GIFR to the west and northern British Isles to the east. The Greenland lithosphere has a cold and dense cratonic root to a depth of about 300 km according to both the seismic and gravity data (Fig. 15). The asthenosphere beneath Iceland has a low-velocity and corresponding low-density anomaly of a relatively smaller magnitude (about 15-20 kg m^{-3}). At the east Greenland margin, (profile distance 500-800 km or about -40°E) along the profile the low-density anomalies (above 200 km depth) correlates with the region affected by the Cenozoic volcanism related to the emplacement of the North Atlantic Igneous Province (Fig. 13). Similarly, the high-amplitude low-density

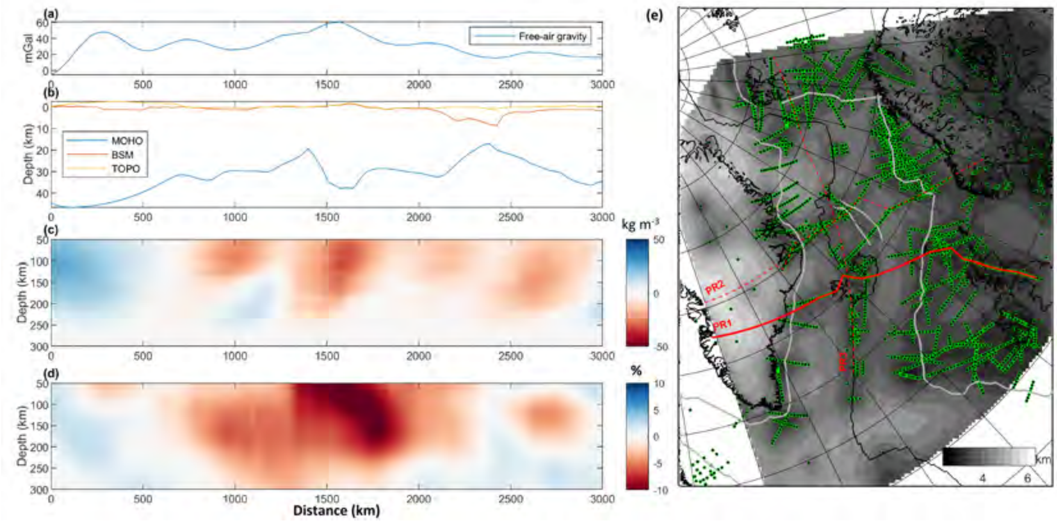

Figure 15. Inversion results along W-E Profile 1 across the northeast Atlantic. (a) Observed free-air gravity anomaly; (b) Crustal geometry: the Moho depth, top basement and topography; (c) density variation with respect to the 3D reference model; (d) seismic shear velocity perturbation in the regional S-wave tomography model (Rickers et al., 2013; Fichtner et al., 2018); (e) the uncertainty of crustal thickness (one standard deviation) with location of seismic refraction profiles (green) and synthetic lithospheric transects (red).

anomaly at the northern Britain margin (profile distance 2300-3000 km or about -12°E) corresponds to Paleocene volcanic centers in the Faeroes region. This density anomaly is outlined by the Caledonian suture zone. A possible explanation for a negative density anomaly beneath the Caledonian deformation front can be related to thin lithosphere and/or the presence of trapped oceanic crust which can be rich in plagioclase at elevated lithospheric temperatures. The lithospheric density structure of GIFR can be related to ultramafic melts crystallized at or below the Moho in combination with fragments of continental lithosphere and/or pyroxenite-rich mantle (Yuan et al., 2020; Foulger et al., 2019).

4.1.2 Profile 2

Profile 2 (Fig. 16) generally follows the previously compiled lithospheric transect across the North Atlantic by Mjelde et al. (2008). The central and east Greenland lithosphere have a contrasting density structure in the model. In the upper lithosphere, the P-wave velocity of thick continental crust thickness of central-east Greenland ($>$ 35 km) was constrained based on the analysis of broadband seismic data (Kraft et al., 2019). The transition to low-density mantle beneath east Greenland margin in Fig. 16b is associated with the shallow lithosphere-asthenosphere boundary in the seismic tomography model (Fig. 16c). The hyper-extended continental crust of Jan Mayen microcontinent (1700 km distance) is underlain by a low-density asthenosphere. This may explain a relatively elevated topography of Jan Mayen (Tan et al., 2017, 2018). The upper mantle beneath the extinct Ægir spreading ridge (A. Breivik et al., 2014) has coincident low-density and low-velocity anomalies (profile distance 2000 km). The shallow lithosphere of the continental margin of Norway appears with a similar positive anomalous density as the Greenland lithosphere whereas the seismic velocities are relatively low here.

As in Profile 1, the correlation of the lithospheric low-density anomalies with the distribution of Cenozoic volcanism is observed along Profile 2. The density image sug-

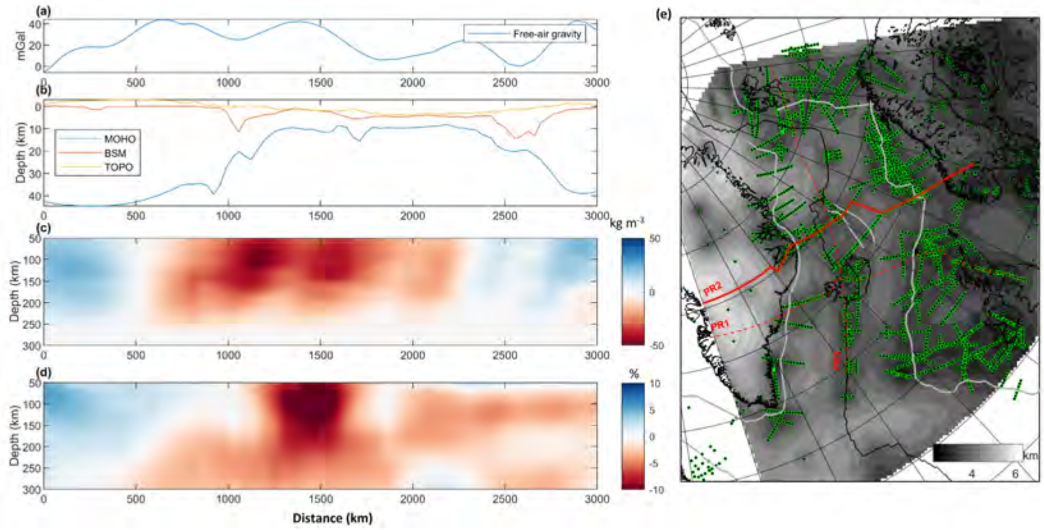

Figure 16. Inversion results along W-E Profile 2 across the northeast Atlantic. (a) Observed free-air gravity anomaly; (b) Crustal geometry: the Moho depth, top basement and topography; (c) density variation with respect to the 3D reference model; (d) seismic shear velocity perturbation in the regional S-wave tomography model (Rickers et al., 2013; Fichtner et al., 2018); (e) the uncertainty of crustal thickness (one standard deviation) with location of seismic refraction profiles (green) and synthetic lithospheric transects (red).

gests that the low-density mantle anomaly beneath the East Greenland margin and the Jan Mayen region has the same deep asthenospheric source. The density and seismic velocity structure suggests branching of a deep thermal anomaly in the shallow upper mantle towards east Greenland and the mid-Atlantic Ridge.

4.1.3 Profile 3

Profile 3 approximately follows the Mid-Atlantic Ridge (Fig. 17), across Iceland (500-1100 km) and Jan Mayen microcontinent (1500-1600 km) and ends at the passive margin of Svalbard. The segmentation of igneous crustal thickness along Profile 3 can be associated with the alternation of low-density and low-shear velocity anomalies in the asthenosphere. This variation can be linked to the excess crustal accretion at the spreading ridge influenced by the Iceland hotspot (A. J. Breivik et al., 2008; Tan et al., 2018; Ito, 2001). The low density anomaly is obtained in the mantle both north and south of Iceland. A deep-seated density anomaly north of Iceland might extend over large distance in the shallow asthenosphere towards Svalbard margin where thin lithosphere is predicted using various geophysical data (Vagnes & Amundsen, 1993; Minakov, 2018; Selway et al., 2020). The intense low-velocity in the upper 100 km beneath the thick igneous crust of Iceland (Gudmundsson, 2003) does not correspond a similar low-density anomaly in Fig. 17. This result should be interpreted with caution since it might also reflect the insufficient resolution in the shallow lithosphere beneath Iceland using the single-component linear gravity gradient inversion we have applied to produce the density image in Fig. 17c. Incorporating other gravity gradient components and/or additional geophysical data can be helpful to further constrain the density structure in this region.

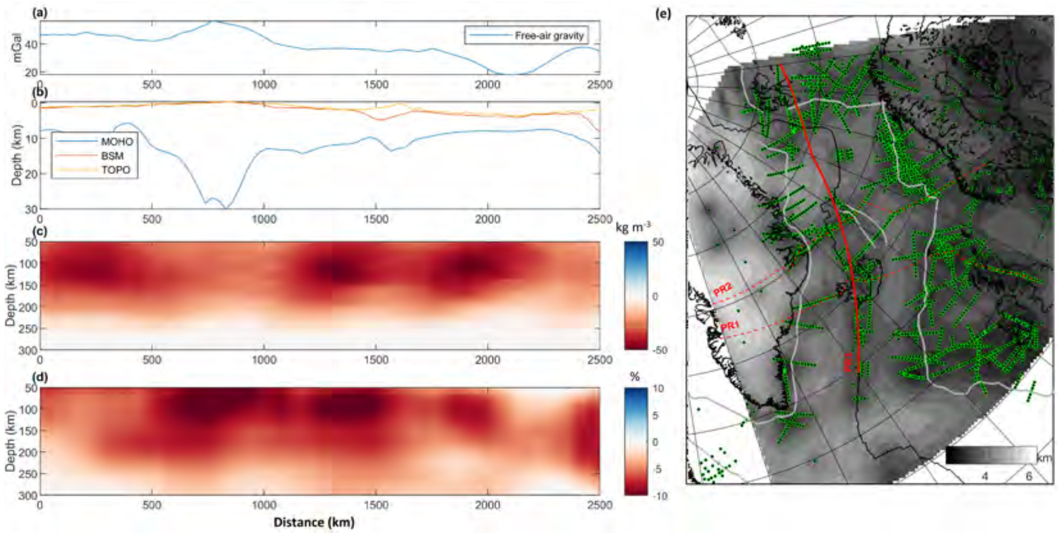

Figure 17. Inversion results along S-N Profile 3 across the northeast Atlantic. (a) Observed free-air gravity anomaly; (b) Crustal geometry: the Moho depth, top basement and topography; (c) density variation with respect to the 3D reference model; (d) seismic shear velocity perturbation in the regional S-wave tomography model (Rickers et al., 2013; Fichtner et al., 2018); (e) the uncertainty of crustal thickness (one standard deviation) with location of seismic refraction profiles (green) and synthetic lithospheric transects (red).

4.2 Relation between density and seismic velocity anomalies

The density structure of the upper mantle is an important parameter for numerical modeling of the lithosphere evolution and for understanding the present-day distribution of lithospheric stresses. The geophysical properties of the upper mantle can be estimated using mineral physics calculations along the lithospheric geotherm e.g. (Stixrude & Lithgow-Bertelloni, 2005). The relation between the seismic velocity and density variations can be established based on their temperature partial derivatives ($\delta\rho/\delta T$, $\delta v_s/\delta T$). The conversion coefficient ($\delta\rho/\delta v_s$) is about 0.2 for adiabatic mantle and a realistic range of chemical composition (Karato, 2008). The deviation of the actual relation between the density anomaly and seismic velocity perturbation from the theoretical value 0.2 increases as the local geotherm deviates from the mantle adiabat.

The joint probability density of the mean density perturbation ($d\rho/\rho_0$) and the seismic velocity perturbation (dv/v_0) for the three selected profiles (shown in Fig. 18) indicates that the theoretical relation $\delta\rho/\delta v_s \approx 0.2$ is recovered for a young oceanic lithosphere for the velocity perturbation -3 to +2 %. For a more pronounced negative velocity anomalies (-3% to -8%) the maximum of joint probability distribution shifts toward smaller $d\rho/\rho_0$ values. This can be interpreted in terms of presence of melt since its direct effect on density is negligible compared to the attenuation of seismic shear velocities.

4.3 Model resolution and uncertainty

The diagonal elements of the posterior covariance matrix provide variance of the resulting density model. Fig. 19 indicates the maximum variance reduction at the depth of about 150 km. The prior model covariance is assumed constant of 400 kg^{2}m^{-6}. The maximum variance reduction is about 250 kg^{2}m^{-6}. The variance reduction with depth

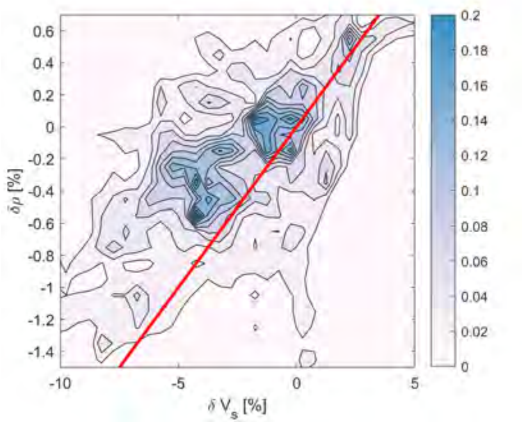

Figure 18. The joint probability density function for the seismic velocity variation and density variation (mean model expressed as a percentage) in the upper mantle. The depth range is 50-250 km. The reference mantle density is 3400 kg m^{-3}. The red line corresponds to the theoretical density-velocity conversion coefficient for adiabatic mantle $\partial_T \rho / \partial_T v = 0.2$.

reflects the shape of the weighted integrated kernel in eq. (63). The largest sensitivity is located at the depths of 100-150 km, which makes the method sensitive to the variation of the lithosphere-asthenosphere boundary geometry.

Our probabilistic inversion approach implies that the density variation in the target region is a result of a Gaussian process. The estimated mean realization of this process is shown in Fig. 13. A way to evaluate the density model parameter space is to generate an ensemble of random realizations using the posterior covariance. This approach can help to test various geological hypotheses proposed in recent publications against interpretation of the GOCE gravity gradient data, such as the composition and nature of the GIFR lithosphere (Foulger et al., 2019; Yuan et al., 2020). A random realization can be constructed using Cholesky decomposition of the covariance matrix and a random vector eq. (49). Six random models (shown in Fig. 20) are centered at the estimated mean model whereas the variance is 150-400 kg^{2}m^{-6} depending on the depth. The full exploration requires a much larger number of realization. Here, we just demonstrate the length scales and the general pattern of more robust features such as the anomalous low-density mantle beneath mid-Atlantic ridge and a high-denser lithosphere of the Fennoscandian craton. The model density variations in the asthenosphere have a sheet-like structure where the low-density material extends over the oceanic basin towards the passive margins.

5 Conclusions

Satellite gravity gradients contain useful information on the density structure of the crust and upper mantle. In this work, we present a probabilistic linear inversion method to image the density heterogeneity within the lithosphere and sub-lithospheric upper mantle. The prior information is incorporated through the spatial (depth) weighting of the model and the data and the model covariance functions, estimated using spherical geostatistical analysis of independent models based on seismological data. This approach provides a novel approach for constrained linear inversion of satellite gravity gradient data in three dimensions.

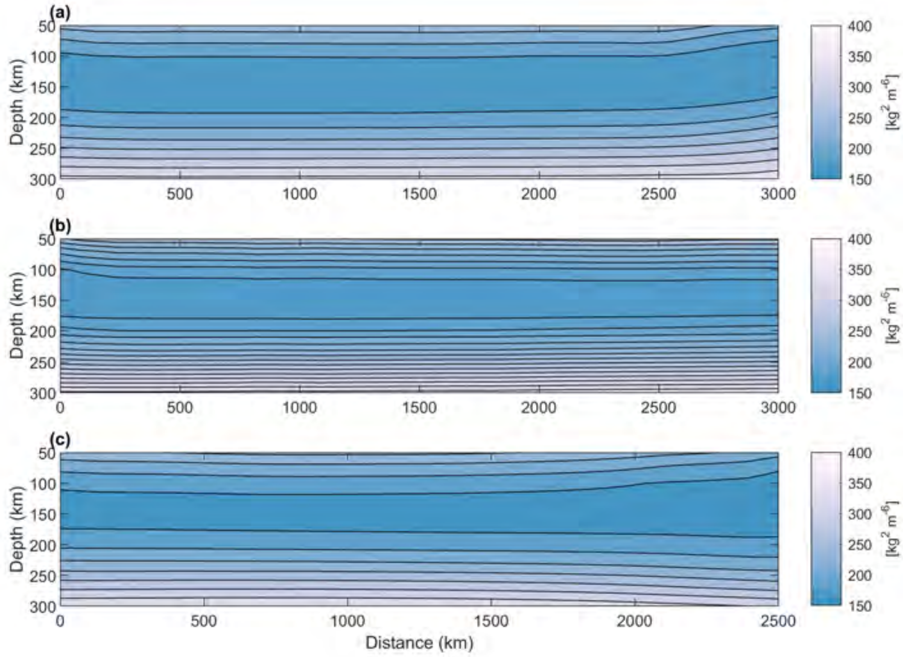

Figure 19. Diagonal elements of the posterior covariance matrix. (a) Profile 1, (b) Profile 2, (c) Profile 3. For location of transects see Fig. 13

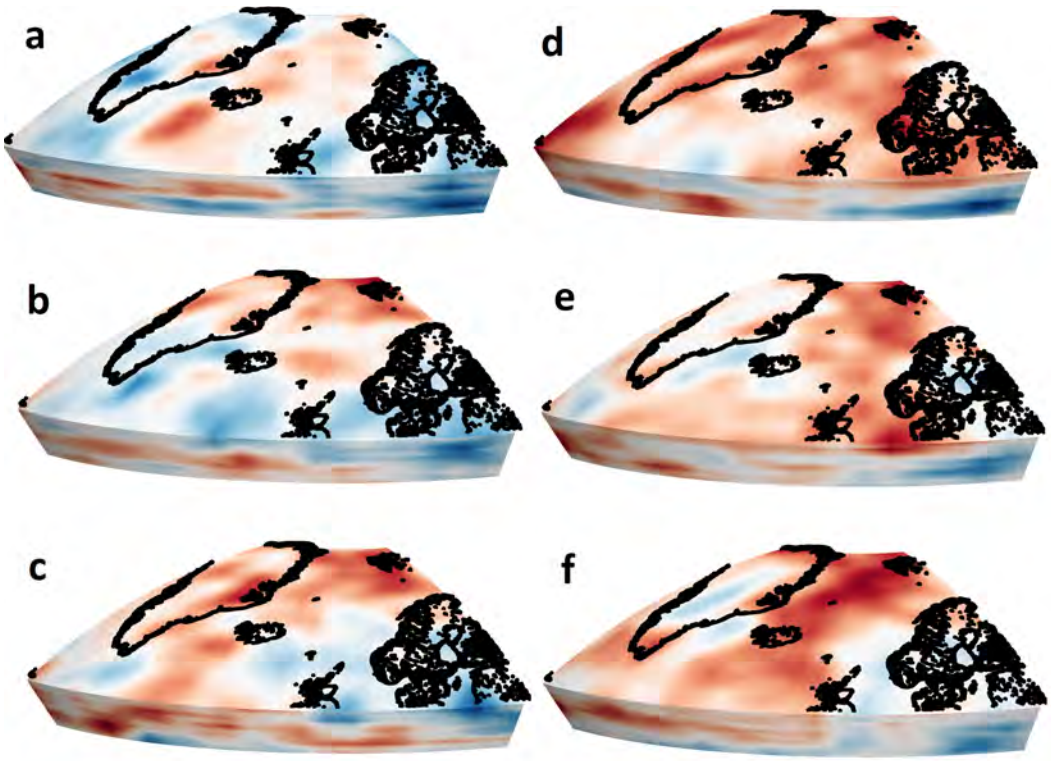

Figure 20. Ensemble of six random realizations generated with the Cholesky decomposition of the posterior covariance matrix. The color scale is from -50 to 50 kg m^{-3}.

The following density features has been resolved in our model for the northeast Atlantic upper mantle. A low-density asthenosphere north and south of Iceland (20-40 $\mathrm{kg\,m^{-3}}$) correlate with the distribution of Cenozoic seamounts and seamount-like features of the ocean floor. No strong low-density anomaly is observed under the present-day location of Iceland. The lithosphere beneath the Greenland-Iceland-Faeroe Ridge appears on average denser relative to the background mantle. The predicted density variation in the upper mantle is generally consistent with seismic velocity anomalies implying a mostly thermal origin of density heterogeneities.

Acknowledgments

This work is done in the framework of the European Space Agency's Support to Science Element program, project "3D Earth: A Living Dynamics Planet". The research is performed at The Centre for Earth Evolution and Dynamics, University of Oslo, funded by the Research Council of Norway through its center of excellence funding scheme, project 223272. The global spherical harmonic analysis was performed using toolbox SHBUNDLE (v. 4/11.2018) by N. Sneeuw et. al., the Institute of Geodesy (GIS), University of Stuttgart: `http://www.gis.uni-stuttgart.de/research/projects`. The XGM gravity model is derived trough the ICGEM web service (Barthelmes, 2013; Ince et al., 2019).

References

Afonso, J. C., Salajegheh, F., Szwillus, W., Ebbing, J., & Gaina, C. (2019). A global reference model of the lithosphere and upper mantle from joint inversion and analysis of multiple data sets. *Geophysical Journal International*, *217*(3), 1602–1628.

Artemieva, I. M., & Thybo, H. (2013). Eunaseis: A seismic model for moho and crustal structure in europe, greenland, and the north atlantic region. *Tectonophysics*, *609*, 97–153.

Aster, R. C., Borchers, B., & Thurber, C. H. (2018). *Parameter estimation and inverse problems*. Elsevier.

Barnoud, A., Coutant, O., Bouligand, C., Gunawan, H., & Deroussi, S. (2016). 3-D linear inversion of gravity data: Method and application to Basse-Terre volcanic island, Guadeloupe, Lesser Antilles. *Geophysical Journal International*, *205*(1), 562–574. doi: 10.1093/gji/ggw030

Barthelmes, F. &. K. (2013). International Centre for Global Earth Models (ICGEM). *Journal of Geodesy, The Geodesists Handbook*.

Barton, P. J. (1992). LISPB revisited: a new look under the Caledonides of northern Britain. *Geophysical Journal International*. doi: 10.1111/j.1365-246X.1992.tb00881.x

Bijwaard, H., & Spakman, W. (1999). Tomographic evidence for a narrow whole mantle plume below Iceland. *Earth and Planetary Science Letters*. doi: 10.1016/S0012-821X(99)00004-7

Boulanger, O., & Chouteau, M. (2001). Constraints in 3D gravity inversion. *Geophysical Prospecting*, *49*(2), 265–280. doi: 10.1046/j.1365-2478.2001.00254.x

Bouman, J., Ebbing, J., & Fuchs, M. (2013). Reference frame transformation of satellite gravity gradients and topographic mass reduction. *Journal of Geophysical Research: Solid Earth*, *118*(2), 759–774. doi: 10.1029/2012JB009747

Bouman, J., Ebbing, J., Meekes, S., Fattah, R. A., Fuchs, M., Gradmann, S., ... Bosch, W. (2015). GOCE gravity gradient data for lithospheric modeling. *International Journal of Applied Earth Observation and Geoinformation*, *35*(PA), 16–30. Retrieved from `http://dx.doi.org/10.1016/j.jag.2013.11.001` doi: 10.1016/j.jag.2013.11.001

Breivik, A., Faleide, J. I., Mjelde, R., Flueh, E., & Murai, Y. (2014). Magmatic development of the outer Vøring margin from seismic data. *Journal of Geophysi-*

cal Research: Solid Earth. doi: 10.1002/2014JB011040

Breivik, A. J., Faleide, J. I., & Mjelde, R. (2008). Neogene magmatism northeast of the Aegir and Kolbeinsey ridges, NE Atlantic: Spreading ridge-mantle plume interaction? *Geochemistry, Geophysics, Geosystems*, *9*(2). doi: 10.1029/2007GC001750

Brown, E. L., & Lesher, C. E. (2014). North Atlantic magmatism controlled by temperature, mantle composition and buoyancy. *Nature Geoscience*, *7*(11), 820–824. Retrieved from `http://www.nature.com/doifinder/10.1038/ngeo2264` doi: 10.1038/ngeo2264

Chasseriau, P., & Chouteau, M. (2003). 3D gravity inversion using a model of parameter covariance. *Journal of Applied Geophysics*, *52*(1), 59–74. doi: 10.1016/S0926-9851(02)00240-9

Cochran, J. R., & Talwani, M. (1978). Gravity anomalies, regional elevation, and the deep structure of the north atlantic. *Journal of Geophysical Research: Solid Earth*, *83*(B10), 4907–4924.

Dahl-Jensen, T., Larsen, T. B., Woelbern, I., Bach, T., Hanka, W., Kind, R., ... Gudmundsson, O. (2003). Depth to Moho in Greeland: Receiver-function analysis suggests two proterozoic blocks in Greenland. *Earth and Planetary Science Letters*. doi: 10.1016/S0012-821X(02)01080-4

Darbyshire, F. A., Bjarnason, I. T., White, R. S., & Flóvenz, Ó. G. (1998). Crustal structure above the Iceland mantle plume imaged by the ICEMELT refraction profile. *Geophysical Journal International*. doi: 10.1046/j.1365-246X.1998.00701.x

Eldholm, D., & Grue, K. (1994). North Atlantic volcanic margins: dimensions and production rates. *Journal of Geophysical Research*. doi: 10.1029/93JB02879

Fichtner, A., van Herwaarden, D.-P., Afanasiev, M., Simutė, S., Krischer, L., Çubuk-Sabuncu, Y., ... others (2018). The collaborative seismic earth model: generation 1. *Geophysical research letters*, *45*(9), 4007–4016.

Foulger, G. R., Doré, T., Emeleus, C. H., Franke, D., Geoffroy, L., Gernigon, L., ... Stoker, M. (2019). A continental Greenland-Iceland-Faroe Ridge. *Earth-Science Reviews*. doi: 10.1016/j.earscirev.2019.102926

Funck, T., Geissler, W. H., Kimbell, G. S., Gradmann, S., Erlendsson, Ö., McDermott, K., & Petersen, U. K. (2017). Moho and basement depth in the NE Atlantic Ocean based on seismic refraction data and receiver functions. *Geological Society, London, Special Publications*, *447*(1), 207–231. Retrieved from `http://sp.lyellcollection.org/content/early/2016/07/12/SP447.1.abstracthttp://sp.lyellcollection.org/lookup/doi/10.1144/SP447.1` doi: 10.1144/SP447.1

Gaina, C., Blischke, A., Geissler, W. H., Kimbell, G. S., & Erlendsson, O. G. (2017). Seamounts and oceanic igneous features in the NE Atlantic: A link between plate motions and mantle dynamics. *Geological Society Special Publication*. doi: 10.1144/SP447.6

Gaina, C., Nasuti, A., Kimbell, G. S., & Blischke, A. (2017). Break-up and seafloor spreading domains in the NE Atlantic. *Geological Society Special Publication*. doi: 10.1144/SP447.12

GEBCO. (2019). *The gebco 2019 grid - a continuous terrain model of the global oceans and land.* [Online]. Available from: `https://www.gebco.net/data_and_products/gridded_bathymetry_data/gebco_2020/`. British Oceanographic Data Centre, National Oceanography Centre, NERC, UK. doi: 10.5285/836f016a-33be-6ddc-e053-6c86abc0788e

Gudmundsson, Ó. (2003). The dense root of the Iceland crust. *Earth and Planetary Science Letters*. doi: 10.1016/S0012-821X(02)01110-X

Haase, C., Ebbing, J., & Funck, T. (2016). A 3D regional crustal model of the NE Atlantic based on seismic and gravity data. *Geological Society, London, Special Publications*, SP447.8. Retrieved from `http://sp.lyellcollection.org/`

lookup/doi/10.1144/SP447.8 doi: 10.1144/SP447.8
Hjartarson, Á., Erlendsson, Ö., & Blischke, A. (2017). The Greenland-Iceland-Faroe Ridge complex. *Geological Society Special Publication*. doi: 10.1144/SP447.14
Hosseini, K., Sigloch, K., Tsekhmistrenko, M., Zaheri, A., Nissen-Meyer, T., & Igel, H. (2020). Global mantle structure from multifrequency tomography using P, PP and P-diffracted waves. *Geophysical Journal International*. doi: 10.1093/gji/ggz394
Ince, E. S., Barthelmes, F., Reißland, S., Elger, K., Förste, C., Flechtner, F., & Schuh, H. (2019). ICGEM – 15 years of successful collection and distribution of global gravitational models, associated services and future plans. *Earth System Science Data Discussions*. doi: 10.5194/essd-2019-17
Ito, G. (2001, jun). Reykjanes "V"-shaped ridges originating from a pulsing and dehydrating mantle plume. *Nature*, *411*(6838), 681–684. Retrieved from http://dx.doi.org/10.1038/35079561
Jakovlev, A. V., Bushenkova, N. A., Koulakov, I. Y., & Dobretsov, N. L. (2012). Structure of the upper mantle in the Circum-Arctic region from regional seismic tomography. *Russian Geology and Geophysics*, *53*(10), 963–971. Retrieved from http://dx.doi.org/10.1016/j.rgg.2012.08.001 doi: 10.1016/j.rgg.2012.08.001
Jones, S. M., White, N., & Maclennan, J. (2002). V-shaped ridges around Iceland: Implications for spatial and temporal patterns of mantle convection. *Geochemistry, Geophysics, Geosystems*, *3*(10), 1–23. Retrieved from http://dx.doi.org/10.1029/2002GC000361 doi: 10.1029/2002GC000361
Karato, S.-i. (2008). *Deformation of earth materials: An introduction to the rheology of solid earth.* Cambridge Press Cambridge.
Kolyukhin, D., & Minakov, A. (2020). Statistic modeling of earth's mantle heterogeneity. *(in review) The International Journal of Geomathematics*, *1*(1), 1-1.
Korenaga, J., Holbrook, W. S., Kent, G. M., Kelemen, P. B., Detrick, R. S., Larsen, H.-C., ... Dahl-Jensen, T. (2000). Crustal structure of the southeast Greenland margin from joint refraction and reflection seismic tomography. *Journal of Geophysical Research: Solid Earth*. doi: 10.1029/2000jb900188
Kraft, H. A., Thybo, H., Vinnik, L. P., & Oreshin, S. (2019). Crustal structure in central-eastern greenland from receiver functions. *Journal of Geophysical Research: Solid Earth*, *124*(2), 1653–1670.
Kumar, P., Kind, R., Priestley, K., & Dahl-Jensen, T. (2007). Crustal structure of Iceland and Greenland from receiver function studies. *Journal of Geophysical Research: Solid Earth*. doi: 10.1029/2005JB003991
Lantuéjoul, C., Freulon, X., & Renard, D. (2019). Spectral simulation of isotropic gaussian random fields on a sphere. *Mathematical Geosciences*, *51*(8), 999–1020.
Laske, G., Masters, G., Ma, Z., & Pasyanos, M. (2013). Update on CRUST1.0—A 1-degree global model of Earth's crust. In *Egu general assembly 2013.*
Last, B., & Kubik, K. (1983). Compact gravity inversion. *Geophysics*, *48*(6), 713–721.
Lebedev, S., Schaeffer, A. J., Fullea, J., & Pease, V. (2018). Seismic tomography of the arctic region: Inferences for the thermal structure and evolution of the lithosphere. In *Geological society special publication* (Vol. 460, pp. 419–440). doi: 10.1144/sp460.10
Legendre, C. P., Meier, T., Lebedev, S., Friederich, W., & Viereck-Götte, L. (2012). A shear wave velocity model of the European upper mantle from automated inversion of seismic shear and surface waveforms. *Geophysical Journal International*. doi: 10.1111/j.1365-246X.2012.05613.x
Li, Y., & Oldenburg, D. W. (1996, mar). 3-D inversion of magnetic data. *GEOPHYSICS*, *61*(2), 394–408. Retrieved from http://library.seg.org/doi/abs/10.1190/1.1822498https://library.seg.org/doi/10.1190/1.1443968

doi: 10.1190/1.1443968

Liang, Q., Chen, C., & Li, Y. (2014, jun). 3-D inversion of gravity data in spherical coordinates with application to the GRAIL data. *Journal of Geophysical Research: Planets*, *119*(6), 1359–1373. Retrieved from `http://doi.wiley.com/10.1002/2014JE004626` doi: 10.1002/2014JE004626

Martinec, Z. (2014). Mass-density Green's functions for the gravitational gradient tensor at different heights. *Geophysical Journal International*, *196*(3), 1455–1465. Retrieved from `http://gji.oxfordjournals.org/cgi/doi/10.1093/gji/ggt495` doi: 10.1093/gji/ggt495

Martinec, Z., & Fullea, J. (2015). A refined model of sedimentary rock cover in the southeastern part of the congo basin from goce gravity and vertical gravity gradient observations. *International Journal of Applied Earth Observation and Geoinformation*, *35*, 70–87.

McKenzie, D. (1978). Some remarks on the development of sedimentary basins. *Earth and Planetary Science Letters*. doi: 10.1016/0012-821X(78)90071-7

Meschede, M., & Romanowicz, B. (2015). Non-stationary spherical random media and their effect on long-period mantle waves. *Geophysical Journal International*, *203*(3), 1605–1625.

Mikhailov, V., Pajot, G., Diament, M., & Price, A. (2007). Tensor deconvolution: A method to locate equivalent sources from full tensor gravity data. *Geophysics*, *72*(5), I61–I69.

Minakov, A. (2018). Late Cenozoic lithosphere dynamics in Svalbard: Interplay of glaciation, seafloor spreading and mantle convection. *Journal of Geodynamics*. doi: 10.1016/j.jog.2018.09.009

Mjelde, R., Raum, T., Breivik, A. J., & Faleide, J. I. (2008). Crustal transect across the North Atlantic. *Marine Geophysical Research*. doi: 10.1007/s11001-008-9046-9

Monin, A., & Yaglom, A. (1975). *Statistical hydrodynamics, vol. 2.* MIT Press.

Mooney, W. D. (2015). Crust and Lithospheric Structure - Global Crustal Structure. In *Treatise on geophysics: Second edition.* doi: 10.1016/B978-0-444-53802-4.00010-5

Novák, P., & Grafarend, E. W. (2006). The effect of topographical and atmospheric masses on spaceborne gravimetric and gradiometric data. *Studia Geophysica et Geodaetica*. doi: 10.1007/s11200-006-0035-7

Paige, C. C., & Saunders, M. A. (1982). Lsqr: An algorithm for sparse linear equations and sparse least squares. *ACM Transactions on Mathematical Software (TOMS)*, *8*(1), 43–71.

Parkin, C. J., & White, R. S. (2008). Influence of the Iceland mantle plume on oceanic crust generation in the North Atlantic. *Geophysical Journal International*. doi: 10.1111/j.1365-246X.2007.03689.x

Parnell-Turner, R., White, N., Henstock, T., Murton, B., Maclennan, J., & Jones, S. M. (2014). A continuous 55-million-year record of transient mantle plume activity beneath Iceland. *Nature Geoscience*. doi: 10.1038/ngeo2281

Pedersen, L. B., & Rasmussen, T. M. (1990). The gradient tensor of potential field anomalies: some implications on data collection and data processing of maps. *Geophysics*, *55*(12), 1558–1566. doi: 10.1190/1.1442807

Pilidou, S., Priestley, K., Debayle, E., & Gudmundsson, Ó. (2005). Rayleigh wave tomography in the North Atlantic: High resolution images of the Iceland, Azores and Eifel mantle plumes. *Lithos*, *79*(3-4 SPEC. ISS.), 453–474. doi: 10.1016/j.lithos.2004.09.012

Pilkington, M. (2014). Evaluating the utility of gravity gradient tensor components. *Geophysics*, *79*(1), G1–G14.

Portniaguine, O., & Zhdanov, M. S. (1999). Focusing geophysical inversion images. *Geophysics*, *64*(3), 874–887.

Raum, T., Mjelde, R., Berge, A. M., Paulsen, J. T., Digranes, P., Shimamura, H.,

... Johnson, M. (2005). Sub-basalt structures east of the Faroe Islands revealed from wide-angle seismic and gravity data. *Petroleum Geoscience*. doi: 10.1144/1354-079304-627

Richards, M., Contreras-Reyes, E., Lithgow-Bertelloni, C., Ghiorso, M., & Stixrude, L. (2013). Petrological interpretation of deep crustal intrusive bodies beneath oceanic hotspot provinces. *Geochemistry, Geophysics, Geosystems*. doi: 10.1029/2012GC004448

Rickers, F., Fichtner, A., & Trampert, J. (2013, apr). The Iceland–Jan Mayen plume system and its impact on mantle dynamics in the North Atlantic region: Evidence from full-waveform inversion. *Earth and Planetary Science Letters*, *367*, 39–51. Retrieved from `http://linkinghub.elsevier.com/retrieve/pii/S0012821X13000897` doi: 10.1016/j.epsl.2013.02.022

Root, B. (2020). Comparing global tomography-derived and gravity-based upper mantle density models. *Geophysical Journal International*, *221*(3), 1542–1554.

Root, B. C., Novák, P., Dirkx, D., Kaban, M., van der Wal, W., & Vermeersen, L. L. (2015). On a spectral method for forward gravity field modelling. *Journal of Geodynamics*. doi: 10.1016/j.jog.2016.02.008

Rudge, J. F., Shaw Champion, M. E., White, N., McKenzie, D., & Lovell, B. (2008, mar). A plume model of transient diachronous uplift at the Earth's surface. *Earth and Planetary Science Letters*, *267*(1-2), 146–160. Retrieved from `http://linkinghub.elsevier.com/retrieve/pii/S0012821X07007674` doi: 10.1016/j.epsl.2007.11.040

Schaeffer, A., & Lebedev, S. (2013). Global shear speed structure of the upper mantle and transition zone. *Geophysical Journal International*, *194*(1), 417–449.

Schoonman, C. M., White, N. J., & Pritchard, D. (2017). Radial viscous fingering of hot asthenosphere within the Icelandic plume beneath the North Atlantic Ocean. *Earth and Planetary Science Letters*, *468*, 51–61. doi: 10.1016/j.epsl.2017.03.036

Sebera, J., Haagmans, R., Floberghagen, R., & Ebbing, J. (2017, nov). Gravity Spectra from the Density Distribution of Earth's Uppermost 435 km. *Surveys in Geophysics*. Retrieved from `http://link.springer.com/10.1007/s10712-017-9445-z` doi: 10.1007/s10712-017-9445-z

Selway, K., Smirnov, M. Y., Beka, T., O'Donnell, J., Minakov, A., Senger, K., ... Kalscheuer, T. (2020). Magnetotelluric constraints on the temperature, composition, partial melt content, and viscosity of the upper mantle beneath svalbard. *Geochemistry, Geophysics, Geosystems*, *21*(5), e2020GC008985.

Shulgin, A., & Artemieva, I. M. (2019). Thermochemical heterogeneity and density of continental and oceanic upper mantle in the european-north atlantic region. *Journal of Geophysical Research: Solid Earth*, *124*(8), 9280–9312.

Sneeuw, N. (1994). Global spherical harmonic analysis by least-squares and numerical quadrature methods in historical perspective. *Geophysical Journal International*, *118*(3), 707–716.

Staples, R. K., White, R. S., Brandsdóttir, B., Menke, W., Maguire, P. K. H., & McBride, J. H. (1997). Färoe-Iceland Ridge Experiment 1. Crustal structure of northeastern Iceland. *Journal of Geophysical Research: Solid Earth*. doi: 10.1029/96jb03911

Stixrude, L., & Lithgow-Bertelloni, C. (2005). *Thermodynamics of mantle minerals - I. Physical properties.* doi: 10.1111/j.1365-246X.2005.02642.x

Straume, E. O., Gaina, C., Medvedev, S., Hochmuth, K., Gohl, K., Whittaker, J. M., ... Hopper, J. R. (2019). GlobSed: Updated Total Sediment Thickness in the World's Oceans. *Geochemistry, Geophysics, Geosystems*. doi: 10.1029/2018GC008115

Szwillus, W., Afonso, J. C., Ebbing, J., & Mooney, W. D. (2019). Global Crustal Thickness and Velocity Structure From Geostatistical Analysis of Seismic Data. *Journal of Geophysical Research: Solid Earth*. doi:

10.1029/2018JB016593
Tan, P., Breivik, A. J., Trønnes, R. G., Mjelde, R., Azuma, R., & Eide, S. (2017). Crustal structure and origin of the eggvin bank west of jan mayen, ne atlantic. *Journal of Geophysical Research: Solid Earth*, *122*(1), 43–62.
Tan, P., Sippel, J., Breivik, A. J., Meeßen, C., & Scheck-Wenderoth, M. (2018). Lithospheric control on asthenospheric flow from the iceland plume: 3-d density modeling of the jan mayen-east greenland region, ne atlantic. *Journal of Geophysical Research: Solid Earth*, *123*(10), 9223–9248.
Tarantola, A. (2004). *Inverse problem theory.* Retrieved from `http://www.ipgp.fr/{~}tarantola/Files/Professional/SIAM/InverseProblemTheory.pdf{\%}0Apapers2://publication/uuid/62A7A164-F0E3-4298-AA2B-222FF673BF4E`
Terdik, G., et al. (2015). Angular spectra for non-gaussian isotropic fields. *Brazilian Journal of Probability and Statistics*, *29*(4), 833–865.
Torsvik, T. H., Amundsen, H. E., Trønnes, R. G., Doubrovine, P. V., Gaina, C., Kusznir, N. J., ... Jamtveit, B. (2015). Continental crust beneath southeast Iceland. *Proceedings of the National Academy of Sciences of the United States of America*. doi: 10.1073/pnas.1423099112
Vagnes, E., & Amundsen, H. E. F. (1993). Late cenozoic uplift and volcanism on spitsbergen: Caused by mantle convection? *Geology*, *21*(3), 251–254.
Wan, L., & Zhdanov, M. S. (2013). Iterative migration of gravity and gravity gradiometry data. *Society of Exploration Geophysicists International Exposition and 83rd Annual Meeting, SEG 2013: Expanding Geophysical Frontiers*(6), 1211–1215. doi: 10.1190/segam2013-1036.1
White, N., & Lovell, B. (1997). Measuring the pulse of a plume with the sedimentary record. *Nature*, *4192*(1995), 1995–1998. Retrieved from `http://bullard.esc.cam.ac.uk/{~}basin/pubs/027.pdf` doi: 10.1038/43151
White, R., & McKenzie, D. (1989). Magmatism at rift zones: The generation of volcanic continental margins and flood basalts. *Journal of Geophysical Research*, *94*(B6), 7685. Retrieved from `http://doi.wiley.com/10.1029/JB094iB06p07685` doi: 10.1029/JB094iB06p07685
Wieczorek, M. A. (2007). Gravity and topography of the terrestrial planets. *Planets and Moons*, 165–206.
Wieczorek, M. A., & Phillips, R. J. (1998, jan). Potential anomalies on a sphere: Applications to the thickness of the lunar crust. *Journal of Geophysical Research: Planets*, *103*(E1), 1715–1724. Retrieved from `http://doi.wiley.com/10.1029/97JE03136` doi: 10.1029/97JE03136
Wild-Pfeiffer, F. (2008). A comparison of different mass elements for use in gravity gradiometry. *Journal of Geodesy*, *82*(10), 637–653.
Yuan, X., Korenaga, J., Holbrook, W. S., & Kelemen, P. B. (2020). Crustal structure of the Greenland-Iceland Ridge from joint refraction and reflection seismic tomography. *Journal of Geophysical Research: Solid Earth*. doi: 10.1029/2020jb019847
Zhdanov, M. S. (2015). *Inverse Theory and Applications in Geophysics*. doi: 10.1016/C2012-0-03334-0
Zhdanov, M. S., Liu, X., Wilson, G. A., & Wan, L. (2011). Potential field migration for rapid imaging of gravity gradiometry data. *Geophysical Prospecting*, *59*(6), 1052–1071. doi: 10.1111/j.1365-2478.2011.01005.x